Article

Cell Reports

Microglial A20 Protects the Brain from CD8 T-Cell-Mediated Immunopathology

Graphical Abstract

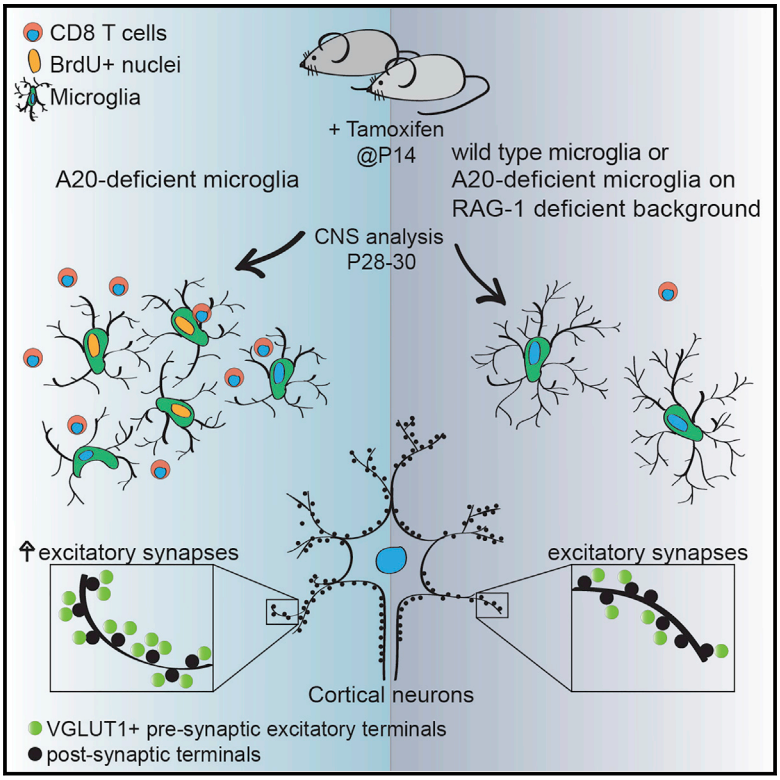

Authors

Alma Nazlie Mohebiany, Nishada Shakunty Ramphal, Khalad Karram, ..., Thomas Mittmann, Doron Merkler, Ari Waisman

Correspondence

waisman@uni-mainz.de

In Brief

A20, as a negative regulator of NF-κB signaling, plays an important role in regulating inflammation. Mohebiany et al. find that A20 in microglia plays a critical role in maintaining CNS homeostasis. When microglia lack A20, immune cells infiltrate the CNS, leading to alterations in microglial structure and neuronal activity.

Highlights

- A20-deficient microglia acquire an inflammatory signature seen in viral infections
- CD8$^+$ T cells infiltrate the CNS when microglia lack A20
- Infiltrating CD8$^+$ T cells are responsible for phenotypic changes in microglia and neurons
- Cortical neurons are hyperactive and have an increased number of synaptic terminals

Mohebiany et al., 2020, Cell Reports *30*, 1585–1597
February 4, 2020
https://doi.org/10.1016/j.celrep.2019.12.097

CellPress

Cell Reports
Article

Microglial A20 Protects the Brain from CD8 T-Cell-Mediated Immunopathology

Alma Nazlie Mohebiany,[1] Nishada Shakunty Ramphal,[1] Khalad Karram,[1] Giovanni Di Liberto,[2] Tanja Novkovic,[3] Matthias Klein,[4] Federico Marini,[5] Mario Kreutzfeldt,[2] Franziska Härtner,[5] Sonja Maria Lacher,[1] Tobias Bopp,[4] Thomas Mittmann,[3] Doron Merkler,[2,6] and Ari Waisman[1,7,*]

[1]Institute for Molecular Medicine, University Medical Center of the Johannes Gutenberg University of Mainz, 55131 Mainz, Germany
[2]Department of Pathology and Immunology, University of Geneva, 1211 Geneva, Switzerland
[3]Institute for Physiology, University Medical Center, Johannes Gutenberg University of Mainz, 55131 Mainz, Germany
[4]Institute for Immunology, University Medical Center of the Johannes Gutenberg University of Mainz, 55131 Mainz, Germany
[5]Institute for Medical Biostatistics, Epidemiology and Informatics (IMBEI), University Medical Center of the Johannes Gutenberg University of Mainz, 55131 Mainz, Germany
[6]Division of Clinical Pathology, Geneva University Hospital, 1211 Geneva, Switzerland
[7]Lead Contact
*Correspondence: waisman@uni-mainz.de
https://doi.org/10.1016/j.celrep.2019.12.097

SUMMARY

Tumor-necrosis-factor-alpha-induced protein 3 (TNFAIP3), or A20, is a ubiquitin-modifying protein and negative regulator of canonical nuclear factor κB (NF-κB) signaling. Several single-nucleotide polymorphisms in *TNFAIP3* are associated with autoimmune diseases, suggesting a role in tissue inflammation. While the role of A20 in peripheral immune cells has been well investigated, less is known about its role in the central nervous system (CNS). Here, we show that microglial A20 is crucial for maintaining brain homeostasis. Without microglial A20, $CD8^+$ T cells spontaneously infiltrate the CNS and acquire a viral response signature. The combination of infiltrating $CD8^+$ T cells and activated A20-deficient microglia leads to an increase in $VGLUT1^+$ terminals and frequency of spontaneous excitatory currents. Ultimately, A20-deficient microglia upregulate genes associated with the antiviral response and neurodegenerative diseases. Together, our data suggest that microglial A20 acts as a sensor for viral infection and a master regulator of CNS homeostasis.

INTRODUCTION

A20 is a key negative regulator of canonical nuclear factor κB (NF-κB) signaling, which mediates its effects via ubiquitin modification of different proteins involved at various levels of the signaling cascade, thereby regulating the pro-inflammatory response induced downstream of NF-κB activation (Baltimore, 2011). Mice fully deficient for A20 die early due to multi-organ inflammation and severe weight loss, partly due to an inability to regulate tumor necrosis factor (TNF)-induced NF-κB signaling (Lee et al., 2000). Therefore, to better understand the role of A20 in inflammation, cell-type-specific deletion of the molecule is necessary. Indeed, aspects of human diseases associated with mutations in *TNFAIP3* can be mimicked by A20 deletion in specific cells (Ma and Malynn, 2012). The role of A20 in peripheral immune cells has been well investigated, but less is known about its role in the central nervous system (CNS). Interestingly, among all CNS-resident cells, microglia express the highest levels of A20 (Zhang et al., 2014).

Microglia are the resident immune cells of the CNS. Under normal conditions, they are highly ramified, and their processes are constantly moving and monitoring their surroundings (Nimmerjahn et al., 2005); thus, they are perfectly poised to rapidly respond to any changes in the homeostasis of the CNS. In addition, they play crucial roles in synapse formation and pruning (Miyamoto et al., 2016; Paolicelli et al., 2011; Schafer et al., 2012), promoting myelination and remyelination (Miron, 2017), and regulating neuronal activity (Li et al., 2012; Wake et al., 2009). Therefore, considering the importance of microglia in the normal functioning of the CNS, we were interested to determine the role of A20 in these cells.

To investigate the role of A20 in microglia, we crossed tamoxifen (TAM)-inducible Cx3cr1-$Cre^{ERT2/+}$ mice to $A20^{fl/fl}$ mice. This system allows microglia-specific deletion of the target gene, as other myeloid cells are replaced with time (Yona et al., 2013). Upon deletion of A20 in microglia, we found a rapid induction of neuroinflammation, characterized by the infiltration of $CD8^+$ T cells and the upregulation of pro-inflammatory molecules by microglia in these A20-deficient ($A20^{\Delta mg}$) mice. Strikingly, both A20-deficient microglia and infiltrating $CD8^+$ T cells acquire a gene expression signature and upregulate genes involved in responding to viral infections. Furthermore, microglial numbers were increased in all regions of the brain examined, associated with alterations in morphology toward decreased complexity.

Furthermore, the deletion of A20 in microglia affected the cortical neurons. Pyramidal neurons displayed altered AMPA-receptor mediated spontaneous excitatory currents associated with a decrease in the density of parvalbumin $(PV)^+$ inhibitory interneurons and an increase in the number of excitatory presynaptic terminals in the cortex. Interestingly, these changes in microglia number and morphology were not observed in $A20^{\Delta mg}$ mice on the $Rag1^{-/-}$ background, which do not have

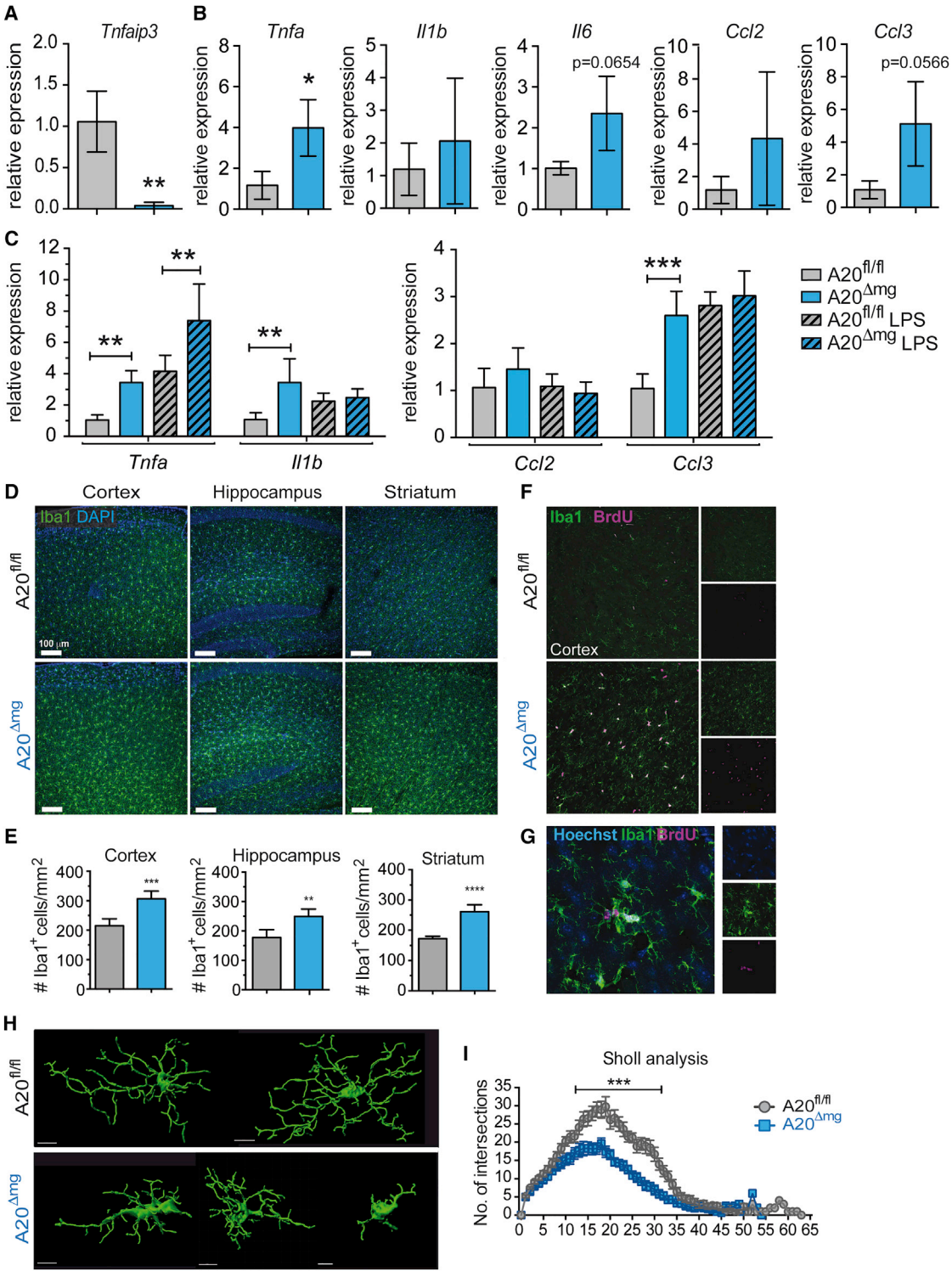

Figure 1. A20-Deficient Microglia Acquire an Inflammatory Phenotype

(A) Expression levels of TNFAIP3 in A20$^{\Delta mg}$ mice 6 weeks after tamoxifen (TAM) injection.

(B) Differential expression of cytokines and chemokines downstream of the NF-κB signaling pathway.

(C) Differential expression of *Tnfa*, *Il1b*, *Ccl2*, and *Ccl3* by cultured microglia with and without LPS stimulation.

(D) Immunofluorescence staining for microglia using Iba1 (green) with DAPI (blue) in cortex, hippocampus, and striatum in A20$^{\Delta mg}$ mice and littermate controls 2 weeks after TAM treatment. Scale bar, 100 μm.

(legend continued on next page)

mature B or T cells. Importantly, increased numbers of excitatory terminals were not observed in the absence of functional RAG enzymes. In summary, our data suggest that microglial A20 is a gatekeeper of CNS homeostasis, and deletion of A20 in microglia imitates the scenario seen following CNS viral infection.

RESULTS

A20-Deficient Microglia Upregulate Pro-inflammatory Molecules

We crossed the $A20^{fl/fl}$ mice to the CX3CR1-Cre^{ERT2} mice and injected $A20^{fl/fl}$ and $A20^{fl/fl}$ CX3CR1-$Cre^{ERT2/+}$ pups with TAM at postnatal day 14 (P14) and P16 by subcutaneous administration, resulting in the translocation of the Cre recombinase to the nucleus of $CX3CR1^{+}$ myeloid cells and subsequent deletion of A20 in these cells. After 6 weeks, we confirmed the deletion of the A20-coding gene (*Tnfaip3*) in microglia isolated from A20-deficient mice, termed here $A20^{\Delta mg}$, by RT-PCR (Figure 1A). We also observed spontaneous upregulation of *Tnfa* and a tendency to upregulate *Il6*, *Ccl2*, and *Ccl3*, but not *Il1b*, in the microglia of the $A20^{\Delta mg}$ mice (Figure 1B), indicating an inflammatory environment in these mice. Since microglia isolation can lead to stress, which alters the RNA expression profile, we cultured and rested microglia from the $A20^{\Delta mg}$ and TAM-treated control mice before analysis. We also examined whether A20-deficient microglia were more sensitive to inflammatory stimuli by adding lipopolysaccharide (LPS). Mirroring the *ex vivo* data, resting microglia from $A20^{\Delta mg}$ mice spontaneously upregulated *Tnfa* expression when compared to control microglia and responded more to LPS stimulation (Figure 1C). Furthermore, *Il-1b* and *Ccl3* expression levels were increased after resting and without stimulation (Figure 1C), confirming an intrinsic inflammatory profile in A20-deficient microglia.

We previously showed that deleting A20 in B cells not only induced a hyperactive phenotype but also enhanced cell proliferation upon activation (Hövelmeyer et al., 2011). Therefore, we expected that the deletion of A20 in microglia, which induces a pro-inflammatory environment in the CNS, would affect their steady state in a similar way. Indeed, when we then analyzed the microglia numbers in the $A20^{\Delta mg}$ mice, we found significantly more $Iba1^{+}$ microglia in the cortex, hippocampus, and striatum of these mice compared to control animals (Figures 1D and 1E). Bromodeoxyuridine (BrdU) feeding for 1 week after TAM administration followed by immunostaining showed that microglia in the cortex of $A20^{\Delta mg}$ mice proliferated during this time (Figure 1F). Small clusters of microglia with BrdU labeling were also identified in the cortex (Figure 1G), while minimal BrdU labeling was seen in control mice. While analyzing the number of microglia, we also noticed that the morphology of the microglia in the $A20^{\Delta mg}$ mice seemed to be altered compared to those of the control mice. We thus performed 3D reconstruction of microglia imaged from the upper layers (layers II/III) of the cortex. This analysis revealed large, well-branched microglia in control mice with a small soma, whereas microglia from $A20^{\Delta mg}$ brains were less branched, approaching a more amoeboid-like appearance (Figure 1H). Sholl analysis on the reconstructed cells quantified and confirmed a significantly decreased branching complexity of A20-deficient microglia (Figure 1I). To determine whether the morphological changes were due to the increased proliferation of microglia in $A20^{\Delta mg}$ mice, we analyzed the morphology of $BrdU^{+}$ and $BrdU^{-}$ microglia from $A20^{\Delta mg}$ mice. Sholl analysis revealed no differences in the cell morphology between $BrdU^{+}$ and $BrdU^{-}$ A20-deficient microglia (Figures S1A and S1B). Therefore, the change in microglial morphology is due to A20 deficiency rather than increased proliferation and secondary alteration in morphology.

Spontaneous Neuroinflammation in Steady State of $A20^{\Delta mg}$ Mice

Next, we analyzed cells isolated from the whole CNS of the $A20^{\Delta mg}$ mice using flow cytometry to determine whether and how the deletion of A20 in microglia affects other cells. Interestingly, we noticed an unusually large population of $CD45^{hi}CD11b^{-}$ cells present in the CNS of $A20^{\Delta mg}$ mice, but not in the control animals (Figures 2A and 2B). Further analysis showed that this population consisted primarily of T cell receptor (TCR) $\beta^{+}CD8^{+}$ T cells, in addition to a smaller population of $CD4^{+}$ T cells (Figures 2C and 2D). This infiltration was specific to the CNS; analysis of immune cells in the lung and gut, which also have A20-deficient $CX3Cr1^{+}$ cells at an early time point after TAM treatment, showed no such infiltration (Figures S2A and S2B). To determine when T cells begin to infiltrate the CNS of these mice, we analyzed the CNS from 1 week up to 1 year after TAM administration. We found that T cells rapidly infiltrate the CNS and are already present from 1 week after the last TAM injection, and they continue to increase in number until the 2-week time point, after which numbers decreased, although they stayed higher than controls even up to 1 year after microglial A20 deletion (Figure 2E). We also confirmed that this 2-week peak was not due to the young age of the mice at the point of TAM administration (i.e., P14) by administering TAM to 8-week-old mice and confirming high $CD8^{+}$ T cell infiltration into the CNS 2 weeks after TAM administration (Figure S2C).

The analysis of the infiltrating $CD8^{+}$ T cells showed them to be effector cells that express high levels of CD44 (Figure 2F), and significantly more of them express CD127 when they first start infiltrating the CNS (Figure 2G). Over time, the expression levels of CD127 decreased (Figure 2G), which, in viral models, is associated with the expansion of effector T cell populations and an

(E) Quantification of microglia numbers 2 weeks after TAM treatment in cortex, hippocampus, and striatum.
(F) Staining for Iba1 (green) and BrdU (magenta) in the cortex of control and $A20^{\Delta mg}$ mice.
(G) Zoomed image of a $BrdU^{+}$ microglia cluster in the cortex of $A20^{\Delta mg}$ mouse.
(H) Representative snapshots from $A20^{\Delta mg}$ mice and littermate controls after 3D reconstruction of microglia imaged from layers II/III of the cortex.
(I) Sholl analysis of reconstructed microglia. N = 4 mice, n = 13 cells for controls; N = 5, n = 15 for $A20^{\Delta mg}$ mice.
Data in bar graphs are represented as mean ± SD. Sholl analysis is shown with mean ± SEM. *$p < 0.05$, **$p < 0.01$, ***$p < 0.001$, and ****$p < 0.0001$, Mann-Whitney test (A–C and E) and two-way ANOVA (I).

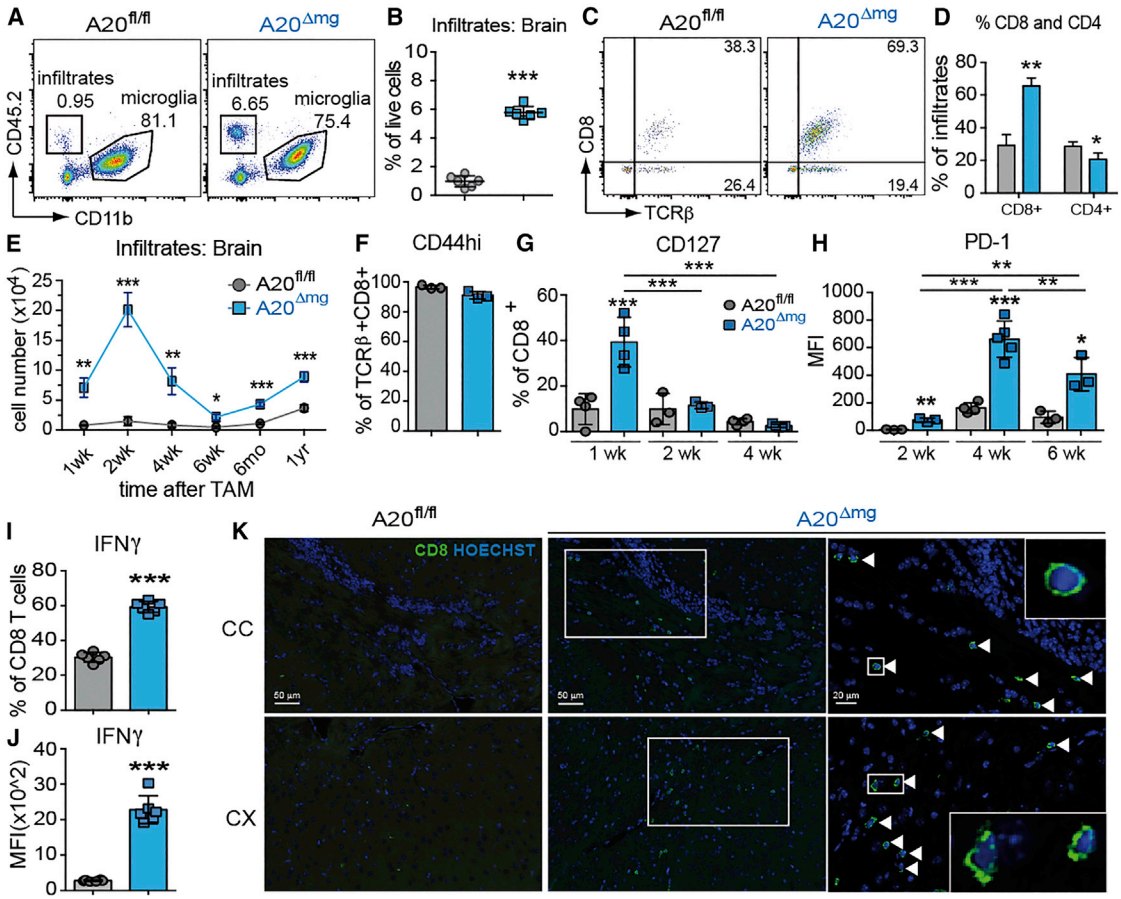

Figure 2. Spontaneous Neuroinflammation in A20$^{\Delta mg}$ Mice

(A) Flow cytometry analysis of mononuclear cells isolated from the brains of A20$^{\Delta mg}$ mice and littermate controls.

(B) Quantification of brain-infiltrating cells (gated on live CD45$^+$CD11b$^-$ cells).

(C) Representative plots of flow cytometry analysis of the CNS from A20$^{\Delta mg}$ mice for infiltrating T cells.

(D) The percentage of CD8$^+$ and CD4$^+$ T cells among TCRβ$^+$ T cells.

(E) Timeline analysis of cell infiltrates in the brain for infiltrates after TAM administration.

(F–J) Expression of CD44 (F), CD127 (G), PD-1 (H), and IFN-γ (I and J) in infiltrating CD8$^+$ T cells isolated from A20$^{\Delta mg}$ mice

(K) Shows CD8$^+$ T cells (green and arrowheads) in the parenchyma of the brain along the corpus callosum (CC) and in the cortex (CX) of A20$^{\Delta mg}$ mice. Scale bars 50 μm and 20 μm (right panel, zoom).

Data are shown as mean ± SD. *p < 0.05, **p < 0.01, and ***p < 0.001, Mann-Whitney test (B, E, I, and J) and two-way ANOVA (G and H).

increased susceptibility to apoptosis (Bachmann et al., 2005). In contrast, PD-1 expression increased with time (Figure 2H), implying exhaustion of these cells. However, upon stimulation, a greater proportion of the infiltrating CD8$^+$ T cells from A20$^{\Delta mg}$ animals produced interferon γ (IFN-γ) compared to controls (Figures 2I and 2J), indicating that the infiltrating T cells are still responsive rather than exhausted. Interestingly, analysis of the TCR V-beta (Vβ) repertoire of infiltrating CD8$^+$ T cells by flow cytometry at the 2-week time point shows a polyclonal expansion of CD8$^+$ T cells expressing TCR Vβ 2, 7, 8.1/8.2, and 13 specifically in the brain compared to the TCR Vβ repertoire found in the spleens of the same or control mice, which we confirmed in two independent experiments (Figure S2D). Lastly, we performed immunostaining on paraffin-embedded sections to determine the localization of the infiltrating CD8$^+$ T cells in the CNS of A20$^{\Delta mg}$ mice. We found CD8$^+$ T cells not only in the meninges (pia) and choroid plexus (Figures S2E and S2F) but also within the parenchyma, infiltrating along the corpus callosum and into the cortex (Figure 2K).

A20-Deficient Microglia Display a Highly Inflammatory Signature

We found that deletion of A20 in microglia led to the invasion of the CNS by CD8$^+$ T cells. Therefore, we decided to investigate what alterations were induced by the A20 deletion in microglia in an attempt to understand how microglia could be mediating the immunological changes observed. To do this, we crossed the mice with eYFP (enhanced yellow fluorescent protein)-reporter mice and isolated eYFP-expressing microglia from control (A20$^{fl/wt}$ eYFP$^{+/-}$ CX3CR1Cre$^{ERT2/+}$) and eYFP$^{+/-}$ A20$^{\Delta mg}$

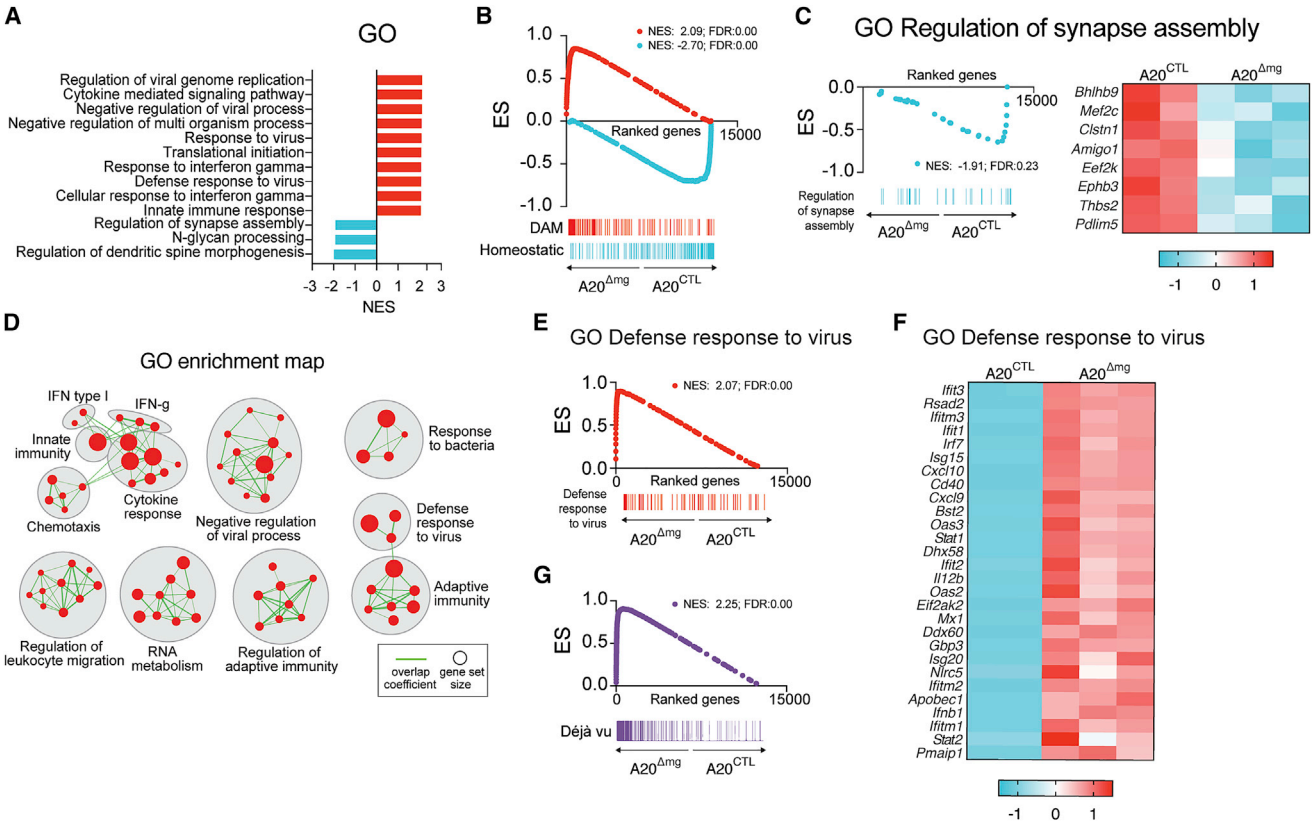

Figure 3. A20-Deficient Microglia Display an Inflammatory Signature Characteristic of the Defense Response to Virus

(A) Gene set enrichment analysis (GSEA) with compiled modules from Gene Ontology (GO). False discovery rate (FDR) <0.25, normalized enrichment score (NES) >1.5.

(B) Enrichment signature comparing microglia from A20$^{\Delta mg}$ mice with the signature of disease associated microglia and microglia in a homeostatic state (DAM; Keren-Shaul et al., 2017).

(C) Enrichment signature and heatmap of differentially expressed genes involved in synaptic assembly.

(D) Enrichment Map network of enriched GO terms showing an upregulation of enriched gene sets related to response to interferons, chemotaxis, defense response against pathogens, and regulation of adaptive immunity.

(E) Enrichment signature comparing microglia from control and A20$^{\Delta mg}$ mice with the signature of the defense response to virus.

(F) Heatmap of differentially expressed genes associated with the defense response to virus.

(G) Enrichment signature of microglia from A20$^{\Delta mg}$ and control mice compared to signature genes upregulated by activated microglia in a model of T cell-mediated encephalitis (déjà vu model).

mice 2 weeks after TAM injection and performed RNA sequencing (RNA-seq). Principal-component analysis of the top 5,000 expressed genes shows differential clustering of the control and the A20$^{\Delta mg}$ samples (Figure S3A). An MA plot of all detected genes shows many differentially expressed genes (red) in the A20-deficient microglia compared to controls (Figure S3B). We focused our analysis on pathways that were altered and performed a gene set enrichment analysis (GSEA). This, along with compiled modules from Gene Ontology (GO) (Ashburner et al., 2000), revealed an upregulation of gene signatures related to antiviral responses, cytokine production, and response to IFN-γ in the microglia of A20$^{\Delta mg}$ mice (Figure 3A; false discovery rate [FDR] < 0.25, normalized enrichment score [NES] > 1.5). We also found that A20-deficient microglia share signature genes with neurodegenerative disease-associated microglia (DAM; Keren-Shaul et al., 2017) but downregulate genes typically associated with homeostatic resting microglia (Figure 3B), further underlining the importance of A20 expression in microglia to maintain homeostasis in the CNS. Interestingly, we also found downregulation of genes involved in synaptic assembly (Figure 3C). Next, we generated an Enrichment Map network of the enriched GO terms derived from the GSEA of A20$^{\Delta mg}$ mice relative to A20 control mice. The network analysis reveals an upregulation of densely connected enriched gene sets with roles in response to interferons and chemotaxis, defense response against viruses and bacteria, and the regulation of adaptive immunity (Figure 3D). Furthermore, we found that microglia from A20$^{\Delta mg}$ mice upregulate many genes associated with the response to viruses (Figures 3E and 3F). We could also establish that A20-deficient microglia express signature genes that are highly upregulated by activated microglia in a model of T-cell-mediated encephalitis (viral déjà vu model; Merkler et al., 2006) (Figure 3G). Overall, microglia lacking A20 develop an antiviral gene expression signature and disrupt the homeostasis of the CNS, leading to the infiltration of CD8 T cells.

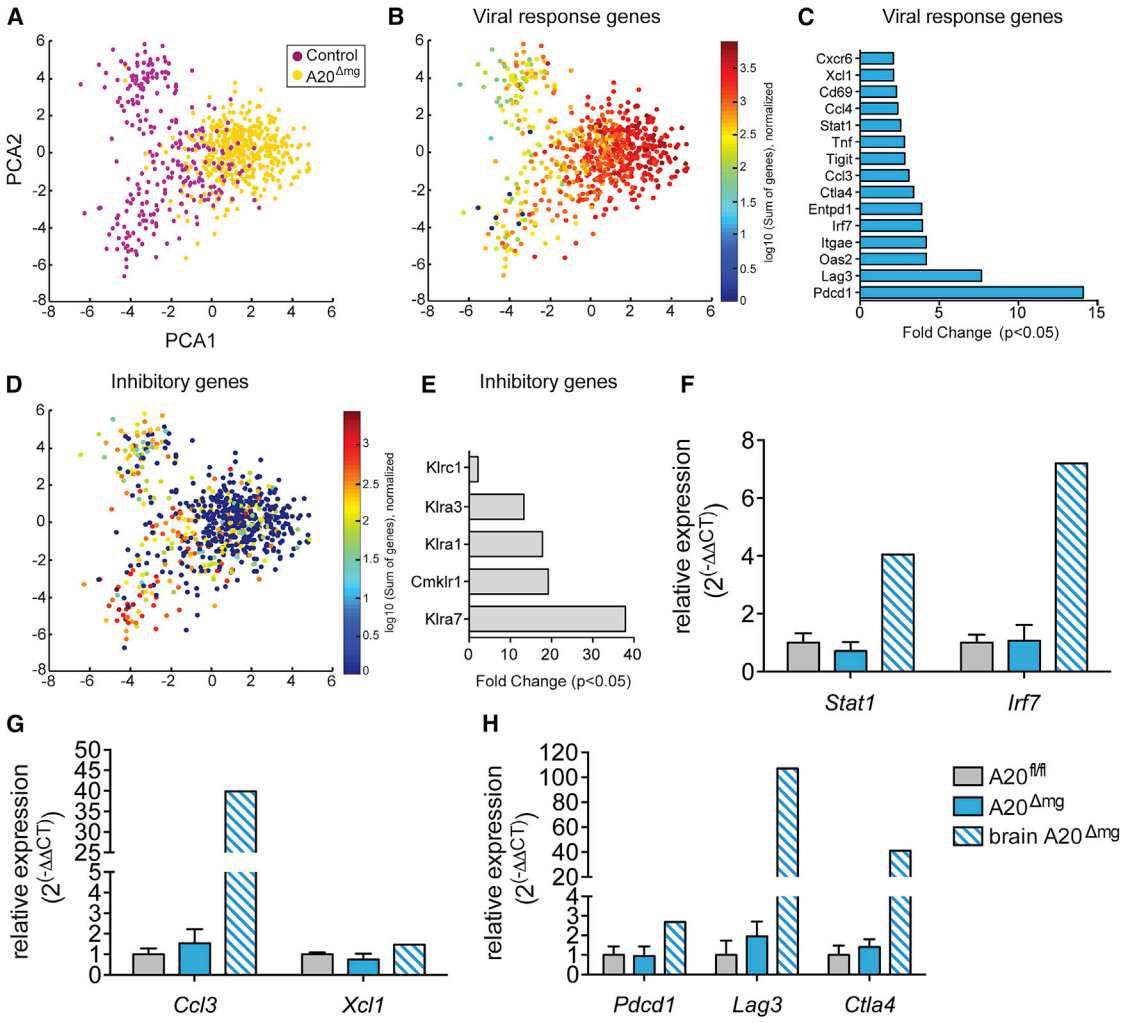

Figure 4. CNS-Infiltrating CD8 T Cells in A20$^{\Delta mg}$ Mice Downregulate Inhibitory Molecules

(A) Single-cell sequencing results of sorted CD8$^+$ T cells from the brains of control (n = 260, N = 3) and A20$^{\Delta mg}$ (n = 440, N = 3) mice. Principal-component analysis plot of all 397 genes found in the BD Rhapsody Immune Response Panel. T cells from control mice in purple, from A20$^{\Delta mg}$ mice in yellow.

(B) Gene expression levels of genes upregulated in CD8$^+$ T cells from brains of A20$^{\Delta mg}$ mice compared to controls overlayed on a principal-component analysis plot.

(C) List of genes upregulated in CD8$^+$ T cells of A20$^{\Delta mg}$ mice.

(D) Gene expression levels of inhibitory genes upregulated in CD8$^+$ T cells from control mice overlayed on a principal-component analysis plot.

(E) List of inhibitory genes expressed in CD8$^+$ T cells from the brains of control mice.

(F–H) qPCR analysis of selected viral-signature genes found in (C) in peripheral CD8$^+$ T cells.

(F) Expression levels of transcription factors Stat1 and Irf7. (G) Expression levels of chemokines Ccl3 and Xcl1.

(H) Expression levels of surface molecules PD-1 (*Pdcd1*), Lag3, and Ctla4. Data in (F)–(H) are shown as mean ± SD. Statistical analysis was performed using multiple t tests and the Holm-Sidak method.

CNS-Infiltrating CD8 T Cells in A20$^{\Delta mg}$ Mice Downregulate Inhibitory Molecules

We then wanted to better understand whether and how the CNS-infiltrating CD8 T cells in A20$^{\Delta mg}$ mice alter their expression profile. Using fluorescence-activated cell sorting (FACS)-isolated CD8 T cells from the brains of control and A20$^{\Delta mg}$ mice, we performed single cell sequencing using the BD Rhapsody Immune Response Panel. We sequenced 260 CD8$^+$ T cells from control brains and 440 cells from A20$^{\Delta mg}$ mice. Principal-component analysis shows that the CD8 T cells from control mice cluster into two groups and that CNS-infiltrating CD8 T cells from A20$^{\Delta mg}$ mice cluster together (Figure 4A). Examination of all upregulated genes in CD8 T cells from A20$^{\Delta mg}$ mice compared to controls shows an increase in the expression of genes related to a (chronic) viral response (Figures 4B and 4C). CD8 T cells from A20-deficient mice upregulate genes such as *Pdcd1*, *Lag3*, *Tigit*, and *Entpd1*, which have all been shown to be associated with chronic viral infections. Furthermore, the IFNg-inducible genes *Cxcl10, Oas2,* and *Stat1* are also significantly upregulated by CNS-infiltrating

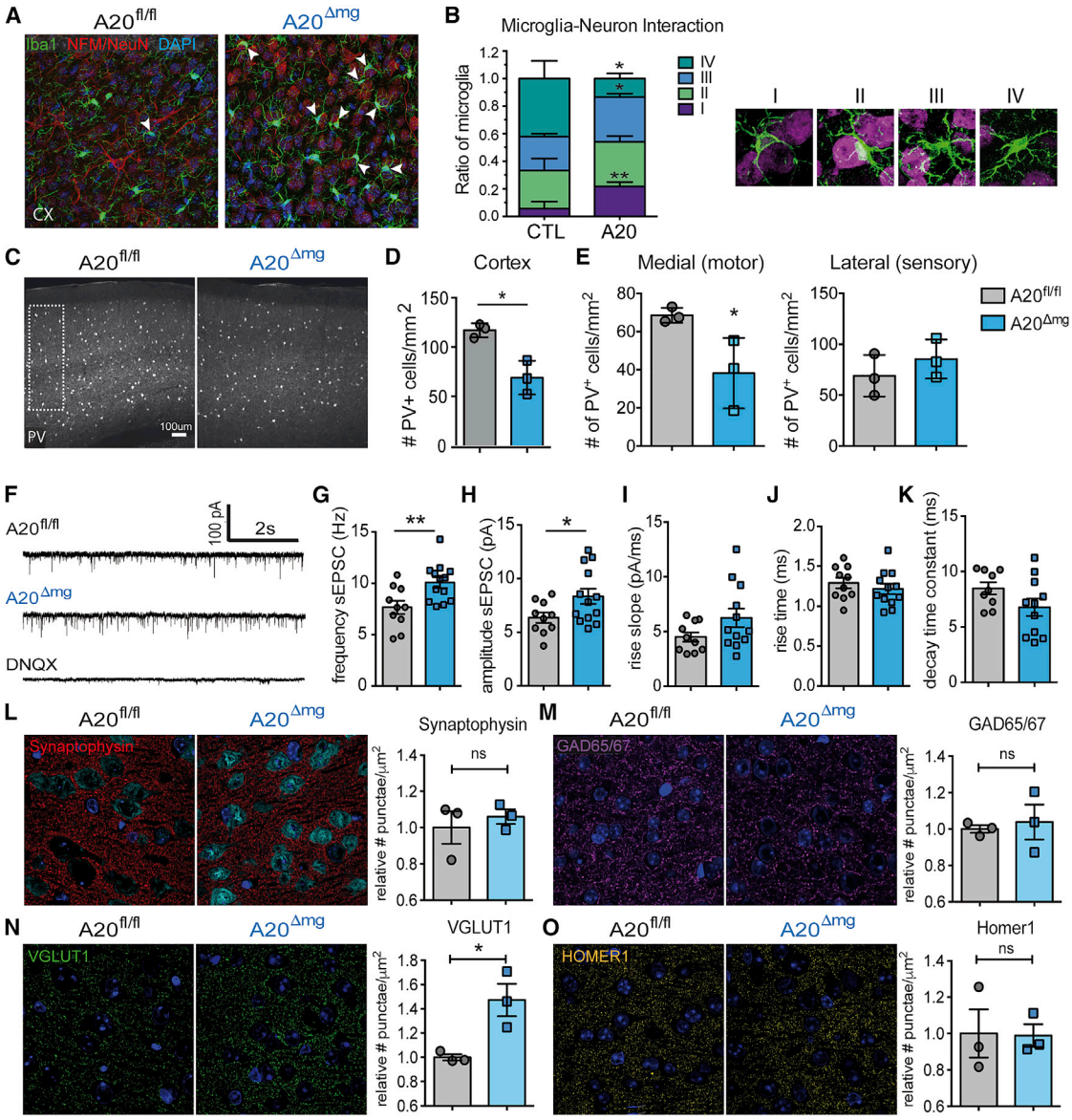

Figure 5. Hyperactivity of Layer III Pyramidal Neurons and Increased Excitatory Presynaptic Terminals in A20$^{\Delta mg}$ Mice

(A and B) Cortical microglia in A20$^{\Delta mg}$ mice contact with neurons.

(A) Overview of cortical microglia (green) and neurons (red) in close contact with neurons (white arrowheads).

(B) Quantification of the interactions between microglia and neurons. I, microglia "hugging" neurons; II, microglia soma in close contact with neuronal soma without hugging; III, microglial branches in close contact with neuronal soma without evidence of soma-soma contact; IV, no evident contact between microglial and neuronal soma in the image.

(C–F) Immunofluorescence staining and quantification of parvalbumin (PV)$^+$ inhibitory interneurons in the cortex.

(C) Representative staining of PV in the cortex with representative counting box (dotted line). Scale bar, 100 μm.

(D and E) Quantification of PV$^+$ interneurons in A20$^{\Delta mg}$ mice compared to controls.

(D) Quantification of cortical PV$^+$ interneurons in cortex (sagittal sections).

(E) Unbiased quantification of PV$^+$ interneurons in motor and somatosensory cortex (coronal sections).

(F) Whole-cell patch-clamp recordings in voltage-clamp mode in acute brain slices of control and A20$^{\Delta mg}$ mice. Representative voltage traces of pharmacologically isolated AMPA-receptor-mediated sEPSCs. Bath application of 6,7-dinitroquinoxaline-2,3-dione (DNQX) abolished all signals, confirming that they were exclusively derived from activation of glutamatergic AMPA receptors.

(G) Quantification of sEPSC frequency in A20$^{\Delta mg}$ mice compared to controls.

(H) Quantification of sEPSC amplitude between the control and A20$^{\Delta mg}$ mice.

(I–K) Quantification of sEPSC rise slope (I), rise time (J), and decay time (K).

(L–O) Quantification of synaptic terminals in layer III of the motor cortex in A20$^{\Delta mg}$ mice compared to littermate controls.

(L) Staining for all synaptic terminals with synaptophysin with quantification.

(legend continued on next page)

CD8 T cells in A20$^{\Delta mg}$ mice (Figure 4C). Interestingly, CNS-patrolling CD8 T cells in control animals express inhibitory genes, which are downregulated in the CNS-infiltrating CD8 T cells of A20$^{\Delta mg}$ mice (Figures 4D and 4E). The inhibitory molecules Klrc1, Klra1, Klra3, and Klra7 are molecules typically expressed by natural killer (NK) cells. Interestingly, the upregulation of viral-signature genes is specific to CNS-infiltrating CD8$^+$ T cells. Analysis of splenic CD8$^+$ T cells by qPCR for selected genes found in Figure 4C shows no similar upregulation of the genes for the transcription factors Stat1 and Irf7 (Figure 4F), the chemokines Ccl3 and Xcl1 (Figure 4G), or the activation/exhaustion markers PD-1, Lag3, and Ctla4 (Figure 4H). This indicates that the viral response signature found in CNS-infiltrating CD8$^+$ T cells is a response localized specifically to the CNS. Overall, we discovered that steady-state CNS-patrolling CD8$^+$ T cells in non-inflammatory conditions show similarities to NK T cells through the expression of inhibitory genes. In A20$^{\Delta mg}$ mice, on the other hand, CNS-infiltrating CD8$^+$ T cells are activated and upregulate genes required for a viral response, similar to what we observed in the microglia.

Altered AMPA-Receptor-Mediated Spontaneous Excitatory Postsynaptic Currents (sEPSCs) in Cortical Pyramidal Neurons of A20$^{\Delta mg}$ Mice

Considering that microglia are heavily involved in forming neuronal networks through their role in synaptic pruning and therefore closely interact with neurons (Miyamoto et al., 2016; Wake et al., 2009), we wanted to examine any functional consequences of microglial activation and CD8 infiltration on neurons in A20$^{\Delta mg}$ mice. Furthermore, RNA-seq of A20-deficient microglia showed a differential expression of genes involved in synapse assembly. Interestingly, during our analysis of microglial morphology, we observed that A20-deficient microglia seemed to be in close contact with neurons as compared to the controls (Figure 5A, arrowheads). Since increased microglia-neuron interactions have been described in inflammatory states, we then imaged microglia and neuronal soma (labeled with Iba1 and NeuN, respectively) from the upper cortical layers to better classify and quantify the microglial-neuronal interactions. We categorized the interactions between microglia and neurons as follows: microglial soma in close contact with neuronal soma with their processes either further enwrapping the neuron (category I) or not (category II), close contact of only microglial processes with neuronal soma (category III), and microglia not in close contact with neurons (Figure 5B). Quantification showed that significantly more A20-deficient microglia enwrapped the neuronal soma with their processes compared to controls (Figure 5B, category I).

Close interactions between microglia and neurons have been shown to be altered in states of inflammation. These interactions lead to either neuroprotection or damage, although the conditions leading to each outcome are not well understood (Gomes-Leal, 2012). On the one hand, it has been shown that microglia in zebrafish react to highly active neurons by increasing contact to neuronal soma (Li et al., 2012), and in a model of traumatic brain injury, microglia closely interacting with neurons remove inhibitory presynaptic terminals, which leads to enhanced synchronized firing and reduced apoptosis of neurons (Chen et al., 2014). On the other hand, a recent publication showing increased microglia-neuron contact in viral infections describes how this interaction can lead to the development of pathology (Di Liberto et al., 2018). Therefore, to investigate possible alterations in the neurons and neuronal populations in A20$^{\Delta mg}$ mice, we first examined the PV-expressing interneuron population of the cortex 2 weeks after TAM administration. We counted the number of PV$^+$ interneurons present in the cortex (excluding layer I, sagittal sections) as outlined in (Figure 5C). Upon quantification, we found a significantly decreased number of PV$^+$ interneurons in the cortex of A20$^{\Delta mg}$ mice as compared to the control animals (Figures 5C and 5D). To determine whether any regional differences were present, we then performed an unbiased analysis on coronal sections, dividing the cortex into medial and lateral areas, containing the motor and somatosensory cortices, respectively. While this analysis revealed no differences in the whole cortex (data not shown), we found a significant reduction in the density of PV$^+$ interneurons in the medial area of the cortex, while no differences were present in the lateral regions (Figure 5E).

To determine whether the changes in microglial morphology, increased microglia contact to neurons, and decreased numbers of PV$^+$ cortical neurons in A20-deficient mice had a functional impact, we analyzed AMPA-receptor-mediated sEPSCs at single pyramidal neurons from layer III in acute cortical brain slices. sEPSCs were pharmacologically isolated and recorded at a holding potential of −80 mV (Figure 5F). We found that the mean frequency of sEPSCs was significantly increased in cells of A20-deficient mice (10.06 ± 0.5 Hz, n = 13) as compared to controls (7.65 ± 0.6 Hz, n = 10, **p < 0.01) (Figure 5G). Moreover, a significant difference in the mean sEPSCs amplitude was evident between A20-deficient mice (8.34 ± 0.7, n = 13) and control mice (6.36 ± 0.4, *p < 0.05) (Figure 5H). However, the comparison of the rise and decay time as well as the rise slope did not disclose any differences between the two groups (Figures 5I–5K). The increased frequency suggested alterations at the presynaptic side; therefore, we analyzed different types of synaptic terminals in layer III of the cortex. A general presynaptic marker, synaptophysin, showed no differences between A20$^{\Delta mg}$ mice and control mice in the numbers of the synapses and the perisomatic terminals (Figure 5L; data not shown). Similar findings were obtained for GAD65/67$^+$ terminals, indicating no changes for GABAergic terminals (Figure 5M; data not shown). On the other hand, staining specifically for excitatory presynaptic terminals with VGLUT1 revealed a significant increase in the number of VGLUT1$^+$ terminals (Figure 5N). However, there were no differences in the number of excitatory postsynaptic terminals identified by Homer1 staining (Figure 5O).

(M) Staining for inhibitory presynaptic terminals with GAD65/67 and quantification of total GAD65/67$^+$ terminals.
(N) Staining for presynaptic excitatory terminals with VGLUT1 and quantification.
(O) Staining for postsynaptic excitatory terminals with Homer1 with quantification.
Data are represented as mean ± SD. *p < 0.05 and **p < 0.01, unpaired t test (PV quantification and electrophysiology) or Mann-Whitney test (synapses).

The increased numbers of VGLUT1^{+} terminals in the cortex of A20$^{\Delta mg}$ mice correlate with the alterations in the sEPSCs, namely the increased frequency. Overall, our findings suggest that the activation state of microglia and the observed neuroinflammation have major consequences for neuronal populations and activity in A20$^{\Delta mg}$ mice, leading to an increased frequency and amplitude of spontaneous glutamatergic currents at pyramidal neurons.

Alterations in Microglia and Neurons Depend on Infiltrating CD8^{+} T Cells

Interestingly, we observed several instances of microglia closely interacting with CD8^{+} T cells (Figures 6A and S4), suggesting an active response by the microglia. Therefore, to determine whether the infiltration of CD8^{+} T cells influences the microglial phenotype, we crossed A20$^{\Delta mg}$ mice to mice lacking the *Rag1* gene and therefore mature T and B cells. Examination of the microglia from the brains of the Rag^{ko} A20$^{\Delta mg}$ mice compared to the Rag^{ko} controls (Rag^{ko} A20$^{fl/fl}$) showed no differences in the numbers of cortical microglia (Figures 6B and 6C). In further contrast to the differences we observed between control and A20$^{\Delta mg}$ mice, the microglia morphology was not altered between Rag^{ko} controls (Rag^{ko} A20$^{fl/fl}$) and Rag^{ko} A20$^{\Delta mg}$ mice, as analyzed using 3D reconstruction and Sholl analysis (Figures 6D and 6E). We then quantified numbers of PV-expressing interneurons of the cortex and again found no differences between control and A20-deficient animals on the Rag^{ko} background (Figure 6F). We also performed an unbiased analysis to quantify PV^{+} interneurons from identical regions of the brain as mentioned previously. There were no differences found in the whole cortex with this analysis, nor was there any difference between genotypes when independently analyzing medial (Figure 6F, right graph) and lateral regions (data not shown). We then examined the synaptic terminals in the cortex of Rag-deficient animals and found no differences in the numbers of synaptic terminals positive for synaptophysin (Figures 6G and 6H), GAD65/67 (Figures 6I and 6J), or VGLUT1 (Figures 6K and 6L) or for Homer 1 (Figures 6M and 6N). Next, since Rag1-deficient mice lack all T cells, in addition to B cells, we depleted CD8 T cells over 3 weeks in control and A20$^{\Delta mg}$ mice to isolate the influence of infiltrating CD8 T cells. After confirming that circulating CD8 T cells were depleted (Figures S5A–S5C), we analyzed the brains for infiltrates. While the A20$^{\Delta mg}$ brains showed no significant increase in the proportion of infiltrating cells (Figures S5D and S5G), the number of cells was still increased in A20-deficient brains. Infiltrates had similar proportions of T cells (Figures S5E and S5H), and further analysis showed that infiltrating CD8^{+} T cells were effectively eliminated (Figures S5F and S5I), although an increased number of CD4^{+} T cells were still present in the brains of A20$^{\Delta mg}$ mice (data not shown). Analysis of microglial number and morphology showed no differences between control and A20$^{\Delta mg}$ brains when CD8 T cells were depleted (Figures 6O–6R). Taken together, the data from Rag-deficient mice and CD8 depletion show that the alterations in morphology and numbers of microglia and the associated alterations in neurons found in the A20$^{\Delta mg}$ mice are not intrinsic but rather an active response to the presence of T cells and/or cytokines produced by these cells.

In summary, upon A20 deletion, microglia develop an inflammatory profile, characterized by the upregulation of chemokines, cytokines, and components involved in the antiviral immune response. This is further accompanied by an increase in microglial numbers and a change in morphology. However, and most strikingly, these changes are not intrinsic to the deletion of A20 in microglia but rather stem from a response to the presence of T cells in the CNS, as the alterations we observed in A20-deficient microglia do not occur in Rag^{ko} A20$^{\Delta mg}$ mice.

DISCUSSION

After deleting A20 in microglia, a sequence of events is initiated, leading to the development of neuroinflammation and affecting the homeostasis of the CNS, characterized by an inflammatory environment and altered microglia morphology, in addition to altered AMPA-mediated currents associated with increased numbers of excitatory synapses in the cortex. Interestingly, a deficiency of the fractalkine receptor, as we have in our A20$^{\Delta mg}$ mice, usually leads to a transient decrease in microglial numbers as well as weaker sEPSC amplitudes. However, these phenotypes are the opposite of what we find in the brains of our A20$^{\Delta mg}$ mice, and it could be that under a different myeloid-specific Cre, we would see a stronger effect as a result of the A20 deletion.

A recent study also describing A20-deficient microglia did not report a similar effect of the A20 deletion on microglia. In contrast to the decreased complexity we observed, the microglia in their animals were more branched compared to controls (Voet et al., 2018), although A20-deficient mice still had increased numbers of microglia. Furthermore, they did not report the presence of infiltrating T cells (Voet et al., 2018), which, in our case, drives the alterations observed in the brains of A20-deficient mice. As the two mutations were very similar in nature, we do not really have an explanation for these differences in results, apart from possible differences in the time of analysis (4 weeks after TAM versus 2 weeks in our study) or differences in the microbiome present in the two different animal facilities. It is also probable that the regions analyzed in the Voet et al. study were not the same between mice; there is no mention of which regions of the brain were used to analyze microglial morphology, for instance, whereas we analyzed microglia from layers II/III of the cortex. As microglia in steady state are not a homogeneous population, it is possible that the differences between the two studies regarding microglial branching arise from this. There is also always the possibility their mice did have infiltrating T cells, but they did not notice this in the course of their analysis. We observed this primarily through flow cytometry analysis in steady state, which is present in the Voet et al. study, but FACS plots are not shown, so we really cannot draw any conclusions.

In our model, peripheral Cx3Cr1-expressing myeloid cells are also deficient for A20 for a short time following TAM injection. As the lack of A20 in peripheral immune cells has previously been shown to have consequences mimicking autoimmune diseases, it is possible that during this time, factors are released that can trigger an inflammatory reaction in microglia, leading to the

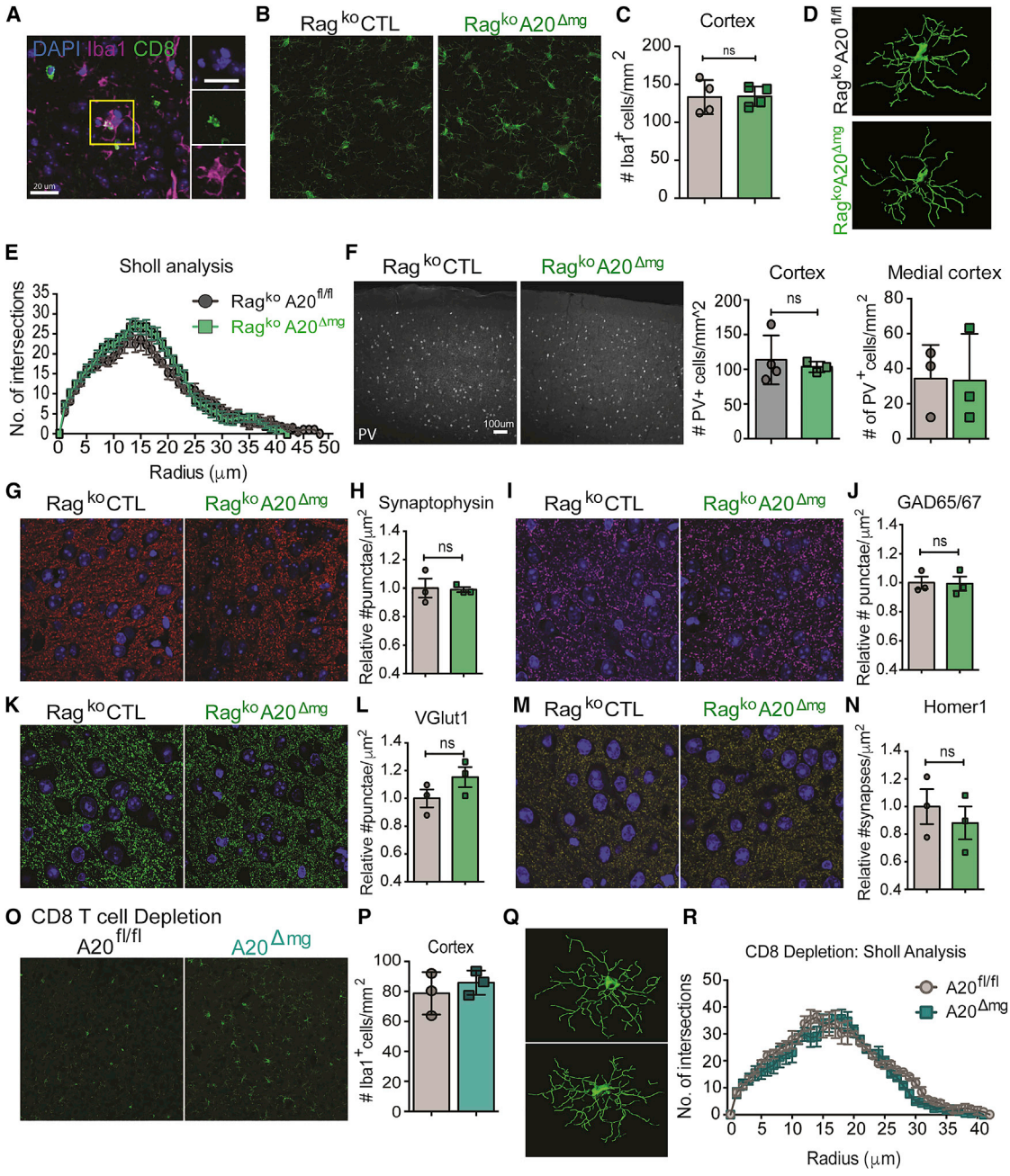

Figure 6. Alterations in Microglia and Neurons Are Dependent on Infiltrating CD8⁺ T Cells

(A) Staining for microglia (Iba1, magenta) and CD8⁺ T cells (green) in paraffin-embedded coronal sections. Representative snapshot showing microglia-CD8⁺ T cell interaction in the cortex. Scale bar 20 μm.

(B) Images of microglia in the cortex of Rag^{ko} CTL and Rag^{ko} A20$^{\Delta mg}$ mice.

(C) Microglial numbers in the cortex of Rag^{ko} A20$^{\Delta mg}$ mice compared to Rag^{ko} A20$^{fl/fl}$ mice.

(D) Representative snapshots of 3D-reconstructed microglia from Rag^{ko} A20$^{\Delta mg}$ mice and controls.

(E) Sholl analysis to quantify branching complexity in Rag^{ko} A20$^{\Delta mg}$ mice compared to littermate controls.

(F) PV staining in cortex of Rag^{ko} A20$^{\Delta mg}$ and control mice and quantification of PV^{+} interneurons in Rag^{ko} A20$^{fl/fl}$ and Rag^{ko} A20$^{\Delta mg}$ mice. Scale bar 100 μm.

(G–N) Quantification of synaptic terminals in layer III of the motor cortex in A20$^{\Delta mg}$ mice compared to littermate controls.

(G and H) Staining for all synaptic terminals with synaptophysin (G), with quantification (H).

(I and J) Staining for inhibitory presynaptic terminals with GAD65/67 (I), and quantification of total GAD65/67^{+} terminals (J).

(K and L) Staining for presynaptic excitatory terminals with VGLUT1 (K), with quantification (L).

(M and N) Staining for postsynaptic excitatory terminals with Homer1 (M), with quantification (N).

(O–R) Microglial analysis after CD8 T cell depletion.

(legend continued on next page)

production of chemokines attracting immune cells to the CNS. While we could not identify a specific signal or signals attracting specifically T cells to infiltrate the CNS, what is interesting to note is that not only IFN-β, but also IFN-γ, the main cytokine produced by the infiltrating $CD8^+$ T cells in A20-deficient mice, can enhance NF-κB signaling in myeloid cells and even sensitize the pathway to weak activating signals (Mitchell et al., 2019). It could be that as $CD8^+$ T cells begin to enter the CNS, they produce IFN-γ, which further enhances NF-κB signaling in microglia, leading to increased production of inflammatory molecules associated to a viral response, further enhancing the entry and activation of $CD8^+$ T cells. This is partly supported by our experiments with $A20^{\Delta mg}$ mice on the $Rag1^{-/-}$ background and the CD8-depletion experiments. Without infiltrating $CD8^+$ T cells in the CNS, there are no alterations in microglial morphology or number, indicating an active role played by $CD8^+$ T cells in affecting microglial activation, possibly through the production of IFN-γ.

Also of interest, normal patrolling $CD8^+$ T cells found in naive animals express inhibitory molecules, which are downregulated by the infiltrating cells in $A20^{\Delta mg}$ mice. It would be of interest to further characterize the expression of inhibitory molecules by CNS-patrolling $CD8^+$ T cells in steady state to better understand their role and how they change and respond to insult.

Most strikingly, A20-deficient microglia upregulate signature genes associated with the response to viral infections, including IFN-β, which has been shown to require NF-κB to be induced (Bartlett et al., 2012), and various IFN-inducible genes. However, the non-canonical NF-κB pathway plays more of a role in the negative regulation of IFN-β (Jin et al., 2014), and thus, the upregulation of IFN and IFN-inducible genes was not necessarily expected. However, what must be considered is that the infiltrating $CD8^+$ T cells in $A20^{\Delta mg}$ mice also strongly upregulate molecules usually seen in viral infections. We would need to do further experiments to determine whether in the absence of $CD8^+$ T cells microglia still upregulate genes related to IFN-inducible genes or the IFN pathway. It could be due to the interaction with $CD8^+$ T cells that microglia develop this gene signature secondary to the deletion of A20, rather than a direct consequence of the loss of A20. However, it is also of interest to note that IFNs are produced in response to viral infections, and a dysregulation in IFN production in the CNS can lead to neuroinflammation and neurological damage (Akwa et al., 1998; Campbell et al., 1999). Astrocytic overexpression of IFN-a led to hyperexcitability of CA1 hippocampal neurons, as well as a loss of PV-containing interneurons (Campbell et al., 1999), similar to what we observe in the cortex of our A20-deficient mice. Overexpression also led to the infiltration of lymphocytes, in particular $CD4^+$ T cells, in addition to $CD8^+$ T cells and B cells (Akwa et al., 1998). In considering an antiviral response, it could be that a focus on IFN signaling and the effects of IFN on the CNS is required to better understand the overall sequence of events in the CNS of A20-deficient mice and look further into the differentially regulated genes in microglia involved in neurodegenerative disease.

It should be noted that NF-κB signaling in microglia under steady-state conditions is active and plays a role in the regulation of synaptic plasticity and neuronal excitability (Kyrargyri et al., 2015). Interestingly, post-mortem and imaging studies of brains from individuals with schizophrenia describe elevated levels of microglia activation (Kenk et al., 2015; Rao et al., 2013), which is associated with an increased expression of pro-inflammatory molecules (Fillman et al., 2013; Rao et al., 2013). Moreover, this activated profile of microglia has been hypothesized to contribute to the deficits in cortical networks observed in patients with schizophrenia (reviewed by Volk, 2017). Also of interest, autoimmune diseases that have been associated with SNPs in *TNFAIP3*, such as rheumatoid arthritis, systemic lupus erythematosus, and psoriasis, are also associated with neurological and psychiatric comorbidities (Amanat et al., 2018; Appenzeller et al., 2006; Joaquim and Appenzeller, 2015). Further considering that CNS viral infections can lead to a number of neurological problems such as epilepsy, which can be modeled by infection with Theiler's murine encephalomyelitis virus (Cusick et al., 2013), and that the release of inflammatory cytokines during viral infection early in development has been associated with the development of autism or schizophrenia in some individuals (Libbey et al., 2005; Mahic et al., 2017; Pearce, 2001), altogether, this could indicate a role for microglia and overactivation of the NF-κB pathway in the development of neurological pathology.

Future studies with the $A20^{\Delta mg}$ mice will need to include an in-depth behavioral analysis to determine the full range of functional consequences of the altered neuronal activity in $A20^{\Delta mg}$ mice and further elucidate the connection between an induced viral response in the CNS and the subsequent development of neuronal pathology. It would also be interesting to see how the $A20^{\Delta mg}$ mice respond to (non-neurotropic) viral infections whether these mice in the end do develop a neurological pathology.

All in all, the deletion of A20 in microglia provides us with a powerful tool to isolate the role of inflammatory microglia in the development of pathology and neuropsychiatric disease, in addition to outlining the critical role A20 and NF-κB signaling play in maintaining CNS homeostasis through its function in microglia.

STAR★METHODS

Detailed methods are provided in the online version of this paper and include the following:

- KEY RESOURCES TABLE
- LEAD CONTACT AND MATERIALS AVAILABILITY
- EXPERIMENTAL MODEL AND SUBJECT DETAILS

(O) Overview of microglia in mice depleted of circulating CD8 T cells.
(P) Quantification of microglial numbers in the cortex of A20 and $A20^{\Delta mg}$ mice after CD8 T cell depletion.
(Q) Representative snapshots of 3D-reconstructed microglia. (R) Sholl analysis of cortical microglia from A20 and $A20^{\Delta mg}$ mice after CD8 T cell depletion.
Data are represented as mean ± SD (bar graphs) and mean ± SEM (Sholl analysis).

SUPPLEMENTAL INFORMATION

Supplemental Information can be found online at https://doi.org/10.1016/j.celrep.2019.12.097.

ACKNOWLEDGMENTS

Support by the IMB Microscopy Core Facility is gratefully acknowledged for use of the Imaris software. We thank Alexander Hoehberg and Sebastian Attig for their assistance with cell sorting. Many thanks to the laboratory of Burkhard Ludewig for providing us with the anti-CD8 antibody. We also thank the laboratory of Krishnaraj Rajalingam for access to their Leica SP8 confocal microscope, and we thank Lisa Johann and Arthi Shanmugavadivu for critical reading of the manuscript. This work was supported by Deutsch Forschungsgemeinschaft (DFG) grants CRC/TR 128 projects A03 and A07 and AW1600/10-1 (to A.W.), CRC1080 TPC02 (to T.M.), and CRC TR128 project B04 (to T.B). A.W. was also financed by EU ITN grant NeuroKine and National Multiple Sclerosis Society (NMSS) grant RG 1707-28780. D.M. was financed by the Swiss National Science Foundation, the Swiss MS Society, and the Helmut Horten Foundation. The Mittmann and Waisman labs are part of the Focus in Translational Neuroscience (FTN) Mainz. A.N.M. received an ESR fellowship under the Marie Curie Action ITN project NeuroKine. A.N.M. and N.S.R. are currently members of the FTN. The Bopp and Waisman labs are part of the Center for Immunotherapy (FZI) Mainz.

AUTHOR CONTRIBUTIONS

A.N.M. generated most of the data and planned experiments. G.D.L. and M.K. performed image acquisition and unbiased quantification of synapses and interneurons. T.N. performed electrophysiological recordings. K.K. assisted with counting of microglia and confocal imaging for IMARIS analysis. N.S.R. performed depletion experiments, CD8 qPCR, immunostaining, and confocal imaging for microglia-BrdU analysis. M.K. and T.B. provided reagents and guided preparation of samples for RNA-seq. F.M., F.H., and G.D.L. performed RNA-seq analysis. S.M.L. assisted with experiments and acquisition of flow cytometry data. F.K., T.M., K.K., and D.M. participated in discussion of results. A.N.M. and A.W. wrote the manuscript. A.W. designed and supervised the study.

DECLARATION OF INTERESTS

The authors declare no competing interests.

Received: August 1, 2019
Revised: December 4, 2019
Accepted: December 27, 2019
Published: February 4, 2020

REFERENCES

Akwa, Y., Hassett, D.E., Eloranta, M.L., Sandberg, K., Masliah, E., Powell, H., Whitton, J.L., Bloom, F.E., and Campbell, I.L. (1998). Transgenic expression of IFN-alpha in the central nervous system of mice protects against lethal neurotropic viral infection but induces inflammation and neurodegeneration. J. Immunol. *161*, 5016–5026.

Amanat, M., Salehi, M., and Rezaei, N. (2018). Neurological and psychiatric disorders in psoriasis. Rev. Neurosci. *29*, 805–813.

Appenzeller, S., Costallat, L.T.L., and Cendes, F. (2006). Neurolupus. Arch. Neurol. *63*, 458–460.

Ashburner, M., Ball, C.A., Blake, J.A., Botstein, D., Butler, H., Cherry, J.M., Davis, A.P., Dolinski, K., Dwight, S.S., Eppig, J.T., et al.; The Gene Ontology Consortium (2000). Gene ontology: tool for the unification of biology. Nat. Genet. *25*, 25–29.

Bachmann, M.F., Wolint, P., Schwarz, K., Jäger, P., and Oxenius, A. (2005). Functional properties and lineage relationship of CD8+ T cell subsets identified by expression of IL-7 receptor alpha and CD62L. J. Immunol. *175*, 4686–4696.

Baltimore, D. (2011). NF-κB is 25. Nat. Immunol. *12*, 683–685.

Bartlett, N.W., Slater, L., Glanville, N., Haas, J.J., Caramori, G., Casolari, P., Clarke, D.L., Message, S.D., Aniscenko, J., Kebadze, T., et al. (2012). Defining critical roles for NF-κB p65 and type I interferon in innate immunity to rhinovirus. EMBO Mol. Med. *4*, 1244–1260.

Campbell, I.L., Krucker, T., Steffensen, S., Akwa, Y., Powell, H.C., Lane, T., Carr, D.J., Gold, L.H., Henriksen, S.J., and Siggins, G.R. (1999). Structural and functional neuropathology in transgenic mice with CNS expression of IFN-α. Brain Res. *835*, 46–61.

Chen, Z., Jalabi, W., Hu, W., Park, H.J., Gale, J.T., Kidd, G.J., Bernatowicz, R., Gossman, Z.C., Chen, J.T., Dutta, R., and Trapp, B.D. (2014). Microglial displacement of inhibitory synapses provides neuroprotection in the adult brain. Nat. Commun. *5*, 4486.

Cusick, M.F., Libbey, J.E., Patel, D.C., Doty, D.J., and Fujinami, R.S. (2013). Infiltrating macrophages are key to the development of seizures following virus infection. J. Virol. *87*, 1849–1860.

Di Liberto, G., Pantelyushin, S., Kreutzfeldt, M., Page, N., Musardo, S., Coras, R., Steinbach, K., Vincenti, I., Klimek, B., Lingner, T., et al. (2018). Neurons under T cell attack coordinate phagocyte-mediated synaptic stripping. Cell *175*, 458–471.e19.

Dobin, A., Davis, C.A., Schlesinger, F., Drenkow, J., Zaleski, C., Jha, S., Batut, P., Chaisson, M., and Gingeras, T.R. (2013). STAR: ultrafast universal RNA-seq aligner. Bioinformatics *29*, 15–21.

Edgar, R., Domrachev, M., and Lash, A.E. (2002). Gene Expression Omnibus: NCBI gene expression and hybridization array data repository. Nucleic Acids Res. *30*, 207–210.

Fillman, S.G., Cloonan, N., Catts, V.S., Miller, L.C., Wong, J., McCrossin, T., Cairns, M., and Weickert, C.S. (2013). Increased inflammatory markers identified in the dorsolateral prefrontal cortex of individuals with schizophrenia. Mol. Psychiatry *18*, 206–214.

Gomes-Leal, W. (2012). Microglial physiopathology: how to explain the dual role of microglia after acute neural disorders? Brain Behav. *2*, 345–356.

Hövelmeyer, N., Reissig, S., Xuan, N.T., Adams-Quack, P., Lukas, D., Nikolaev, A., Schlüter, D., and Waisman, A. (2011). A20 deficiency in B cells enhances B-cell proliferation and results in the development of autoantibodies. Eur. J. Immunol. *41*, 595–601.

Jin, J., Hu, H., Li, H.S., Yu, J., Xiao, Y., Brittain, G.C., Zou, Q., Cheng, X., Mallette, F.A., Watowich, S.S., and Sun, S.C. (2014). Noncanonical NF-κB pathway controls the production of type I interferons in antiviral innate immunity. Immunity *40*, 342–354.

Joaquim, A.F., and Appenzeller, S. (2015). Neuropsychiatric manifestations in rheumatoid arthritis. Autoimmun. Rev. *14*, 1116–1122.

Kenk, M., Selvanathan, T., Rao, N., Suridjan, I., Rusjan, P., Remington, G., Meyer, J.H., Wilson, A.A., Houle, S., and Mizrahi, R. (2015). Imaging neuroinflammation in gray and white matter in schizophrenia: an in-vivo PET study with [18F]-FEPPA. Schizophr. Bull. *41*, 85–93.

Keren-Shaul, H., Spinrad, A., Weiner, A., Matcovitch-Natan, O., Dvir-Szternfeld, R., Ulland, T.K., David, E., Baruch, K., Lara-Astaiso, D., Toth, B., et al. (2017). A unique microglia type associated with restricting development of Alzheimer's disease. Cell *169*, 1276–1290.e17.

Kreutzfeldt, M., Bergthaler, A., Fernandez, M., Bruck, W., Steinbach, K., Vorm, M., Coras, R., Blumcke, I., Bonilla, W.V., Fleige, A., et al. (2013). Neuroprotective intervention by interferon-γ blockade prevents CD8+ T cell-mediated dendrite and synapse loss. J. Exp. Med. *210*, 2087–2103.

Kyrargyri, V., Vega-Flores, G., Gruart, A., Delgado-García, J.M., and Probert, L. (2015). Differential contributions of microglial and neuronal IKKβ to synaptic plasticity and associative learning in alert behaving mice. Glia *63*, 549–566.

Lee, E.G., Boone, D.L., Chai, S., Libby, S.L., Chien, M., Lodolce, J.P., and Ma, A. (2000). Failure to regulate TNF-induced NF-kB and cell death responses in A20-deficient mice. Science *289*, 2350–2354.

Li, Y., Du, X.F., Liu, C.S., Wen, Z.L., and Du, J.L. (2012). Reciprocal regulation between resting microglial dynamics and neuronal activity in vivo. Dev. Cell *23*, 1189–1202.

Libbey, J.E., Sweeten, T.L., McMahon, W.M., and Fujinami, R.S. (2005). Autistic disorder and viral infections. J. Neurovirol. *11*, 1–10.

Love, M.I., Huber, W., and Anders, S. (2014). Moderated estimation of fold change and dispersion for RNA-seq data with DESeq2. Genome Biol. *15*, 550.

Ma, A., and Malynn, B.A. (2012). A20: linking a complex regulator of ubiquitylation to immunity and human disease. Nat. Rev. Immunol. *12*, 774–785.

Mahic, M., Mjaaland, S., Bovelstad, H.M., Gunnes, N., Susser, E., Bresnahan, M., Oyen, A.-S., Levin, B., Che, X., Hirtz, D., et al. (2017). Maternal immunoreactivity to herpes simplex virus 2 and risk of autism spectrum disorder in male offspring. MSphere *2*, e00016–17.

Marini, F., and Binder, H. (2017). Development of applications for interactive and reproducible research: a case study. Genomics Comput. Biol. *3*, 39.

Merkler, D., Horvath, E., Bruck, W., Zinkernagel, R.M., Del la Torre, J.C., and Pinschewer, D.D. (2006). "Viral déjà vu" elicits organ-specific immune disease independent of reactivity to self. J. Clin. Invest. *116*, 1254–1263.

Miron, V.E. (2017). Microglia-driven regulation of oligodendrocyte lineage cells, myelination, and remyelination. J. Leukoc. Biol. *101*, 1103–1108.

Mitchell, S., Mercado, E.L., Adelaja, A., Ho, J.Q., Cheng, Q.J., Ghosh, G., and Hoffmann, A. (2019). An NFκB activity calculator to delineate signaling crosstalk: type I and II interferons enhance NFκB via distinct mechanisms. Front. Immunol. *10*, 1425.

Miyamoto, A., Wake, H., Ishikawa, A.W., Eto, K., Shibata, K., Murakoshi, H., Koizumi, S., Moorhouse, A.J., Yoshimura, Y., and Nabekura, J. (2016). Microglia contact induces synapse formation in developing somatosensory cortex. Nat. Commun. *7*, 12540.

Nimmerjahn, A., Kirchhoff, F., and Helmchen, F. (2005). Neuroscience: resting microglial cells are highly dynamic surveillants of brain parenchyma in vivo. Science *308*, 1314–1318.

Paolicelli, R.C., Bolasco, G., Pagani, F., Maggi, L., Scianni, M., Panzanelli, P., Giustetto, M., Ferreira, T.A., Guiducci, E., Dumas, L., et al. (2011). Synaptic pruning by microglia is necessary for normal brain development. Science *333*, 1456–1458.

Pearce, B.D. (2001). Schizophrenia and viral infection during neurodevelopment: a focus on mechanisms. Mol. Psychiatry *6*, 634–646.

Rao, J.S., Kim, H.W., Harry, G.J., Rapoport, S.I., and Reese, E.A. (2013). Retraction. Increased neuroinflammatory and arachidonic acid cascade markers, and reduced synaptic proteins, in the postmortem frontal cortex from schizophrenia patients. Schizophr. Res. *147*, 24–31.

Schafer, D.P., Lehrman, E.K., Kautzman, A.G., Koyama, R., Mardinly, A.R., Yamasaki, R., Ransohoff, R.M., Greenberg, M.E., Barres, B.A., and Stevens, B. (2012). Microglia sculpt postnatal neural circuits in an activity and complement-dependent manner. Neuron *74*, 691–705.

Srinivas, S., Watanabe, T., Lin, C.S., William, C.M., Tanabe, Y., Jessell, T.M., and Constantini, F. (2001). Cre reporter strains produced by targeted insertion of EYFP and ECFP into the ROSA26 locus. BMC Dev. Biol. *1*. https://doi.org/10.1186/1471-213X-1-4.

Voet, S., Mc Guire, C., Hagemeyer, N., Martens, A., Schroeder, A., Wieghofer, P., Daems, C., Staszewski, O., Vande Walle, L., Jordao, M.J.C., et al. (2018). A20 critically controls microglia activation and inhibits inflammasome-dependent neuroinflammation. Nat. Commun. *9*, 2036.

Volk, D.W. (2017). Role of microglia disturbances and immune-related marker abnormalities in cortical circuitry dysfunction in schizophrenia. Neurobiol. Dis. *99*, 58–65.

Wake, H., Moorhouse, A.J., Jinno, S., Kohsaka, S., and Nabekura, J. (2009). Resting microglia directly monitor the functional state of synapses in vivo and determine the fate of ischemic terminals. J. Neurosci. *29*, 3974–3980.

Yona, S., Kim, K.W., Wolf, Y., Mildner, A., Varol, D., Breker, M., Strauss-Ayali, D., Viukov, S., Guilliams, M., Misharin, A., et al. (2013). Fate mapping reveals origins and dynamics of monocytes and tissue macrophages under homeostasis. Immunity *38*, 79–91.

Zhang, Y., Chen, K., Sloan, S.A., Bennett, M.L., Scholze, A.R., O'Keeffe, S., Phatnani, H.P., Guarnieri, P., Caneda, C., Ruderisch, N., et al. (2014). An RNA-sequencing transcriptome and splicing database of glia, neurons, and vascular cells of the cerebral cortex. J. Neurosci. *34*, 11929–11947.

Zhu, A., Ibrahim, J.G., and Love, M.I. (2018). Heavy-tailed prior distributions for sequence count data: removing the noise and preserving large differences. bioRxiv. https://doi.org/10.1101/303255.

STAR★METHODS

KEY RESOURCES TABLE

REAGENT or RESOURCE	SOURCE	IDENTIFIER
Antibodies		
Rat anti-CD11b PE-Cy7 (Clone M1/70)	eBioscience	Cat# 25-0112; RRID: AB_469588
Rat anti-CD45.2 FITC (Clone 104)	eBioscience	Cat# 11-0454; RRID: AB_465061
Rat anti-CD45 BV510 (Clone 30-F11)	Biolegend	Cat# 103138; RRID: AB_2563061
Armenian hamster anti-TCRbeta FITC (clone H57-597)	Biolegend	Cat# 109205; RRID: AB_313428
Rat anti-CD8 PerCP (Clone 53-6.7)	Biolegend	Cat# 100732; RRID: AB_893423
Rat anti-CD8 Pacific Blue (Clone 53-6.7)	Biolegend	Cat# 100725; RRID: AB_493425
Rat anti-CD44 FITC (Clone IM7)	eBioscience	Cat# 11-0441; RRID: AB_465044
Rat anti-CD127 Biotin (Clone A7R34)	Biolegend	Cat# 135005; RRID: AB_1953262
Armenian hamster anti-PD-1 PE (Clone J43)	eBioscience	Cat# 12-9985; RRID: AB_466294
Rat anti-IFNgamma PE (Clone XMG1.2)	BD Biosciences	Cat# 554412; RRID: AB_395376
Rabbit anti-Iba1 (polyclonal)	WAKO	Cat# 019-19741; RRID: AB_839504
Rat anti-BrdU (clone BU1/75 (ICR1))	Abcam	Cat# ab6326; RRID: AB_305426
Rat anti-mouse CD8a (clone 4SM15)	eBioscience	Cat# 14-0808-80; RRID: AB_2572860
Mouse anti-(medium) Neurofilament (Clone NF-09)	Acris Antibodies GmbH (now OriGene)	Cat# SM3068P; RRID: AB_1005618
Mouse anti-NeuN (Clone A60)	Chemicon/Merk Millipore	Cat# MAB377; RRID: AB_2298772
Rabbit anti-NeuN-Alexafluor 488 (clone EPR12763)	Abcam	Cat# ab190195; RRID: AB_2716282
Rabbit anti-Parvalbumin (antiserum)	Swant	Code# PV27; RRID: AB_2631173
Mouse anti-Synaptophysin (clone 27G12)	Novocastra	Cat# NCL-L-SYNAP-299; RRID: AB_564017
Mouse anti-VGLUT1 (clone A-8)	Santa Cruz	Cat# sc-377425; RRID: AB_2687960
Mouse anti-Homer 1 (clone 26)	Santa Cruz	Cat# sc-136358; RRID: AB_10612905
mouse anti-GAD65/67 (Clone C-9)	Santa Cruz	Cat# sc-365180; RRID: AB_10710523
Goat anti-rat IgG-CF555	Sigma/Biotium	Cat# SAB4600070; RRID: AB_10854235
Goat anti-rabbit-CF488A	Sigma/Biotium	Cat# SAB4600044; RRID: AB_10853801
Goat anti-mouse IgG- F(ab')2 -CF555	Sigma/Biotium	Cat# SAB4600299
Anti-mouse Cy2	Jackson	715-225-151
Goat anti-mouse IgG Alexa Fluor 555	Thermofisher	Cat# A21127
Rat anti-mouse CD8 (Cell line YTS-169.4.2.1)	Purified antibody provided by B. Ludewig (University of Zurich)	N/A
Chemicals, Peptides, and Recombinant Proteins		
DAPI	Invitrogen	Cat# D1306
Hoechst 33342	Invitrogen	Cat#H3570
eFL780 fixable viability dye	eBioscience	Cat# 65-0865-18
BrdU	Sigma	Cat# B5002
Paraformaldehyde solution 4% in PBS	Santa Cruz	Cat# Sc-281692
Tamoxifen	Sigma	Cat# T5648
Papain	Sigma	Cat# P4762
Collagenase Type II	GIBCO	Cat# 17101-015
DNaseI	Roche	Cat# 10104159001
Percoll	GE Healthcare UK	Cat# 17089101
Fluoroshield with DAPI	Sigma	Cat# F6057
PermaFluor Aqueous Mounting Medium	Thermoscientific	Cat# TA-006-FM

(*Continued on next page*)

Continued

REAGENT or RESOURCE	SOURCE	IDENTIFIER
Critical Commercial Assays		
CD11b MicroBeads	Miltenyi	130-049-601
CD8a+ T cell Isolation Kit	Miltenyi	130-104-075
CD45 MicroBeads	Miltenyi	130-052-301
Fixation/Permeabilization Solution kit	BD Biosciences	Cat# 554714
RNeasy plus Mini Kit	QIAGEN	Cat# 74104
NEBNext® Poly(A) mRNA Isolation Module	NEB	Cat# E7490L
NEBNext® Ultra™ II RNA Library Prep Kit for Illumina®	NEB	Cat# E7770L
Deposited Data		
RNA-seq from microglial A20-sufficient and A20-deficient mice in steady state	This paper	GEO: GSE123033
Experimental Models: Organisms/Strains		
Mouse: *A20*$^{fl/fl}$	Hövelmeyer et al., 2011	N/A
Mouse: *Cx3cr1*^{CreERT2}	Yona et al., 2013	N/A
Mouse: *Rosa26*-Stop-*eYFP*	Srinivas et al., 2001	N/A
Mouse: *Rag1*$^{-/-}$	Jackson	N/A
Oligonucleotides		
For mouse *Lag3*, forward 5′CCAGGCCTCGATGATTGCTA3′	Metabion	N/A
For mouse *Lag3*, reverse 5′CAGCAGCGTACACTGTCAGA3′	Metabion	N/A
For mouse *Stat1*, forward 5′GAACGCGCTCTGCTCAA3′	Metabion	N/A
For mouse *Stat1*, reverse 5′TGCGAATAATATCTGGGAAAGTAA3′	Metabion	N/A
For mouse *Irf7*, forward 5′GCCAGGAGCAAGACCGTGTT3′	Metabion	N/A
For mouse *Irf7*, reverse 5′TGCCCCACCACTGCCTGTA3′	Metabion	N/A
For mouse *CTLA4*, forward 5′GCTTCCTAGATTACCCCTTCTGC3′	Metabion	N/A
For mouse *CTLA4*, reverse 5′CGGGCATGGTTCTGGATCA3′	Metabion	N/A
For mouse *Xcl1*, forward 5′TTTGTCACCAAACGAGGACTAAA3′	Metabion	N/A
For mouse *Xcl1*, reverse 5′CCAGTCAGGGTTATCGCTGTG3′	Metabion	N/A
Ccl3	QIAGEN	N/A
Pdcd1	QIAGEN	N/A
Mm Hprt_1_SG QuantiTect primer assay	QIAGEN	QT00166768
Software and Algorithms		
Imaris 8.4	Bitplane	N/A
FlowJo2 (version 10.0)	TreeStar	N/A
FIJI	https://fiji.sc/	N/A
Definiens Developer XD	Definiens	N/A
PClamp 10.1	Molecular Device	N/A
R language and environment for statistical computing and graphics	https://www.r-project.org	N/A
STAR aligner (version 2.4.0j)	https://github.com/alexdobin/STAR/blob/master/CHANGES.md	N/A

(*Continued on next page*)

Continued

REAGENT or RESOURCE	SOURCE	IDENTIFIER
DESeq2 package (version 1.22.1)	https://bioconductor.org/packages/release/bioc/html/DESeq2.html	N/A
Gene set enrichment analysis (GSEA) Desktop Application v2.2.1	https://software.broadinstitute.org/gsea/index.jsp	N/A
Enrichment Map plugin	http://www.baderlab.org/Software/EnrichmentMap	N/A
Cytoscape (version 3.6.0)	https://cytoscape.org	N/A

LEAD CONTACT AND MATERIALS AVAILABILITY

Any further information and requests for reagents or animals should be directed to and will be fulfilled by the lead contact, Ari Waisman (waisman@uni-mainz.de).

This study did not generate new unique reagents.

EXPERIMENTAL MODEL AND SUBJECT DETAILS

All mice used were on the C57BL/6J background and housed under specific-pathogen-free conditions. Cx3cr1-Cre$^{ERT2/+}$ mice[12] were bred to A20$^{fl/fl}$ mice. A20$^{fl/fl}$ Cx3cr1-Cre$^{ERT2/+}$ (A20$^{\Delta mg}$) mice were further crossed to the Rag 1$^{-/-}$ background. For sequencing experiments, A20$^{fl/fl}$ Cx3cr1-Cre$^{ERT2/+}$ mice were further crossed to A20$^{fl/wt}$ eYFP$^{+/+}$ mice to obtain eYFP-positive microglia upon recombination. All animal experiments were performed in accordance with the guidelines from the Central Animal Facility Institution. The mutations were induced at P14 and P16 (see below for treatment), and analyzed at 4 weeks of age, unless otherwise indicated.

METHOD DETAILS

Tamoxifen treatment

A 20 mg/mL solution of tamoxifen (Sigma Aldrich) was prepared by suspension in olive oil (Sigma Aldrich) at 37°C for 2 hours on a shaker. Pups were injected subcutaneously with 2mg of tamoxifen, 2 days apart at P14 and P16.

BrdU treatment

On the same day as the first tamoxifen injection (at P18), mice were given 0.8 mg/mL of BrdU with 1% sucrose (w/v) in their drinking water over a period of 1 week. The water was changed once after 3 days. Mice were then left for an additional week after BrdU treatment, before being sacrificed at the 2 week time point after TAM injection, and brains collected for histology.

Organ isolation

Mice were deeply anesthetized by inhalation with isoflurane then transcardially perfused with 15-20mL NaCl before organs for analysis were removed. For histology: mice were perfused with ice-cold PBS and then with ice-cold 4% PFA. Brains were post-fixed in 4% PFA overnight and further processed for histology. For cell-isolation: Brain and spinal cord were digested using 1mg papain (for microglia analysis; Sigma-Aldrich) in HBSS with calcium and magnesium (Sigma-Aldrich) or Collagenase Type II (for microglia and lymphocyte analysis; GIBCO) for 30min at 37°C, before being passed through a 70μm cell strainer. CNS homogenates were put into a discontinuous 30%:70% percoll gradient and centrifuged without brakes. Myelin was discarded and the interface collected for further processing: either sorting of microglia for qPCR or sequencing; or flow cytometry analysis.

CD8$^+$ T cell depletion

CD8 cells were depleted in three-week-old mice with a depleting anti-CD8 antibody (kind gift from B. Ludewig, Switzerland). 300 μg anti-CD8 was injected i.p. every three days over 2 weeks. The deletion of A20 was induced with TAM two days after the first anti-CD8 injection and the second TAM injection administered two days later. Blood was taken from the tail before and 1 week after anti-CD8 injection and analyzed by flow cytometry to confirm CD8$^+$ T cell depletion. Blood was collected with heparin to prevent clotting, and immune cells isolated with a Ficoll-gradient to remove the erythrocytes. Two weeks after the first tamoxifen injection mice were perfused with PBS, half of the brain was used for histological analysis of microglia and the other half was used for flow cytometry.

Flow cytometry staining: immune cell analysis

Single cell suspensions from the CNS were resuspended in FACS buffer (PBS with 2% FCS) with Fc-block for 20 minutes, washed and stained on ice for 20 min in the dark with a combination of the following stains or antibodies in FACS buffer: viability dye APC-eFl780 (1:1000; eBioscience); anti-CD45.2 FITC (1:1000; eBioscience); anti-CD11b PECy7 (1:1000; eBioscience); anti-TCRβ biotin (1:200; BD Biosciences) and streptavidin PerCP (1:600; Biolegend).

Immunofluorescence/Histology

PFA-fixed brains were embedded in 2% agarose and 40 μm free-floating sagittal sections cut with a vibratome (Leica). Sections were blocked for 1h in D1 buffer (0.5% BSA 0.3% Triton-100 in PBS) at room temperature, then stained overnight with primary antibodies for microglia using rabbit anti-Iba1 (1:800, Wako); neurons using mouse anti-NeuN (1:500, Clone A60, Chemicon), or mouse anti-neurofilament M (1:500, Clone NF-09, Acris Antibodies GmbH).

For BrdU and CD8-Depletion experiments, PFA-fixed brains were transferred to a 30% w/v sucrose solution until they sank (usually after 48h). Brains were then embedded in Tissue-Tek O.C.T. Compound and frozen in a slurry of dry ice and 2-methylbutane. Brains were then cut on a sliding microtome in a cryostat and directly mounted onto Polysine Adhesion Slides (Thermoscientific). For BrdU staining, we performed antigen retrieval in citrate-buffer (10mM Citric Acid, pH 6.0), for 1h in a steamer. After coming to room temperature, slides were denatured using 2N HCl for 1h at room temperature (RT) then non-specific binding blocked for 1h at room temperature (RT) with 10% FCS in PBS. Primary antibodies against Iba-1 and BrdU (1:400, Abcam) were incubated overnight.

For CD8-T cell staining, mice were perfused with saline followed by cold 4% PFA, and overnight post-fixation in 4% PFA. The CNS was isolated and embedded in paraffin, and 3-4 μm thin sections were cut. Staining for Iba-1 and CD8 (eBioscience) was performed on coronal sections after antigen retrieval and blocking unspecific binding.

For all stainings, bound primary antibody was further labeled with the appropriate secondary antibodies. Secondary antibodies were incubated with sections for 1h at RT in blocking buffer: anti-rabbit CF488A (1:800, Sigma-Aldrich); anti-mouse IgG F(ab')2 CF555 (1:300, Sigma Aldrich); anti-rat IgG CF555 (1:500, Sigma Aldrich). Nuclei were further stained either with Hoechst and mounted with PermaFluor Aqueous Mounting Medium (Thermoscientific) or directly mounted with Fluoroshield mounting media with DAPI (Sigma-Aldrich).

Parvalbumin staining and quantification

CNS tissue was fixed with 4% paraformaldehyde (PFA) and embedded in paraffin as described previously (Kreutzfeldt et al., 2013). For immunofluorescence staining, after antigen retrieval (Pascal Citrate pH6) and unspecific binding blocking, PFA-fixed coronal sections were incubated with rabbit anti-Parvalbumin primary antibody (1:8000 dilution). Bound antibodies were visualized with goat anti–rabbit 488 antibody. Sections were then incubated anti-Iba1 rabbit directly labeled 647 antibody (dilution 1:100). Nuclei were stained with DAPI (Invitrogen). Immunostained sections were scanned using Pannoramic 250 FLASH II (3DHISTECH) Digital Slide Scanner with objective magnification of 20x. Positive signals in cortical regions were quantified by a blinded experimenter using an automated custom-made script, which was based on Cognition Network Language (Definiens Cognition Network Technology; Definiens Developer XD software).

Quantification of microglia

40μm free-floating sections were stained with Iba1 and Hoechst as described above. Sections were imaged with an Olympus ix81 fluorescence microscope, with an objective magnification of 20x. Images were acquired from cortex, hippocampus, and striatum. Only microglia with a clear cell body in-focus were counted. For CD8-depletion experiments, 20 μm sagittal sections were stained with Iba-1 as described above and imaged with a Leica Dmi8 fluorescence microscope with an objective magnification of 20x.

Electrophysiological recording

Mice (n = 10) were deeply anesthetized by inhalation with isoflurane and decapitated. The brains were dissected in cold (1 – 4°C), oxygenated, sucrose-based artificial cerebrospinal fluid (aCSF) (in mM: NaCl, 87; KCl, 2.4; KH_2PO_4, 1.25; $MgSO_4$, 2.6; $CaCl_2$, 0.5; d-sucrose, 75 and d-glucose, 10; pH: 7.4). Transversal slices (400 μm) containing the somatosensory cortex were prepared from both hemispheres and incubated at room temperature in an oxygenated sucrose-based aCSF for 1 hour. Single slices were transferred to a recording chamber that was located on the fixed-stage of an upright Olympus-BX50WI microscope (Olympus). The chamber was continuously perfused with standard oxygenated artificial aCSF containing (in mM) NaCl, 124; KCl, 4.9; KH_2PO_4, 1.2; $MgSO_4$, 1.3; $CaCl_2$, 2.5; $NaHCO_3$, 25.6 and d-glucose, 10; pH: 7.4.

Whole-cell patch-clamp recordings were performed in acute cortical slices from pyramidal neurons in layers III. AMPA receptor-dominated sEPSCs were pharmacologically isolated by bath application of picrotoxin (PTX, 50 μM) and D (−)-2-Amino-5-phosphonopentanoic acid (D-AP5, 20 μM) and measured in voltage clamp-mode at −80 mV. The recording glass pipettes (resistance 5 - 7 MΩ) were filled with an intracellular solution containing (in mM) 125 Cs-gluconate, 5 CsCl, 10 EGTA, 2 $MgCl_2$, 2 Na_2-ATP, 0.4 Na_2-GTP, 10 HEPES and 5 QX-314; pH: 7.3. The access resistance was controlled before and after each recording. Neurons were discarded if this parameter was either higher than 20 MΩ or changed more than 20%. An Axopatch-200B amplifier (AXON Instrument) was used to record the electrical signals. The data were filtered at 10 kHz and digitized at 20 kHz using a Digidata-1400 system with PClamp 10 software (Molecular Device,). PClamp 10.1 software was used for offline analysis of the recorded sEPSCs.

Synaptic staining

For synaptic stainings, PFA-perfused CNS tissue was post-fixed in 4% PFA and embedded in paraffin. After antigen retrieval and unspecific binding blocking, PFA-fixed sections were incubated with primary antibodies. Bound antibodies were visualized with appropriate species-specific Cy2- or Cy3- conjugated secondary antibodies. Nuclei were stained with DAPI (Invitrogen). Immunostained sections were scanned using confocal microscope LSM 800 (Zeiss), with objective magnification of 63x, sampling tiles from the layer III of primary motor area, (bits 16, pixel size 0.06 μm).

Primary antibodies: mouse anti-GAD65-67 (clone C-9, 1:100, Santa Cruz Biotechnology), rabbit anti-NeuN (clone EPR12763, Abcam, directly labeled with Alexafluor 488), mouse anti-synaptophysin (clone 27G12,1:50, Novocastra), mouse anti-VGLUT1 (clone A-8, 1:100, Santa Cruz Biotechnology), mouse anti-Homer1 (clone 26, 1:100, Santa Cruz Biotechnology).

Secondary antibodies: anti-mouse Cy2 (Jackson ImmunoResearch Laboratories); anti-mouse Alexafluor 555 (Thermofisher). Secondary antibodies were used at 1:200 dilution.

Quantification of synaptic terminals

To evaluate the number of presynaptic terminals (synaptophysin, GAD65-67, VGLUT1) and postsynaptic terminals (Homer1), positive signals were quantified using a custom-made script, based on Cognition Network Language (Definiens Cognition Network Technology; Definiens Developer XD software). The total tissue area was normalized using DAPI+ signal to ensure similar cellular numbers in the field of view. FIJI software (NIH) was used to enumerate perisomatic synaptophysin (SYP) and GAD65/67 positive boutons.

Microglia reconstruction and Sholl analysis

40 μm free-floating sections were stained for microglia using Iba1 as described above. Images of microglia from layers II/III of the cortex were acquired with a 20x oil-immersion objective with 3x optical zoom, and 1.0 μm increments on a Leica SP8 from the top to the bottom of each slice imaged. Stacks were opened with Imaris 8.4 and processes semi-automatically traced using the Filament tracing tool. Only cells with a cell body in the center of the stack were taken for analysis. To quantify cell complexity, Scholl analysis from Imaris was used on reconstructed cells. For analysis of microglia from BrdU-fed mice, 20 μm mounted cryosections were stained for Iba1 and BrdU as described above. Images of microglia from layers II/III of the cortex were acquired with a 20x oil-immersion objective with 3x optical zoom, and 1.0 μm increments on a Leica SP8 from the top to the bottom of each slice imaged. Stacks were opened with FIJI (NIH). Stacks were merged to identify BrdU+ and BrdU- microglia. To perform Sholl analysis, Iba1 stacks were collapsed using Maximum projection. Threshold was set to the same level for all images. Again only microglia with a cell body at the center of the stack were taken for analysis. The cell body was defined and Sholl Analysis (From Image) was performed. Starting radius was defined as 1 μm from the center, with increments of 1 μm up to 20 μm from the center (the distance at which significant differences were observed in microglial complexity in the 3D analysis using Imaris).

Microglia sorting

Microglia were sorted using Magnetic Activated Cell Sorting (MACS; Miltenyi), with CD11b beads (Miltenyi) according to manufacturer's instructions. Briefly, CNS-isolated cells were incubated with anti-CD11b MACS beads, washed then applied to prepared LS columns. Columns were washed 3x with MACS buffer, before elution of CD11b+ cells. Samples were further processed for RNA extraction and qPCR. For sequencing experiments, microglia from eYFP-A20$^{\Delta mg}$ mice and eYFP-A20$^{fl/wt}$ Cx3cr1-Cre$^{ERT2/+}$ mice were isolated as described above (using papain), and stained with a viability dye, CD45 and CD11b. Microglia were then sorted on a FACS Aria, identified by gating on live, single cells, CD45^{intermediate} CD11b^{+} cells, then eYFP+ cells.

CD8^{+} T cell sorting and sequencing

For sequencing: brains of A20$^{\Delta mg}$ mice and control mice were dissected out and cells isolated as described above (using collagenase), stained with viability dye, CD45, CD11b, CD11c, CD90.2, CD4 and CD8. Each sample was then stained with a unique Sample Tag from BD. Control samples were pooled together, and A20$^{\Delta mg}$ samples were pooled together. CD8^{+} T cells were then sorted out on a FACS Aria, identified by gating on live single cells, CD45^{+} CD11b^{-} cells, CD90.2^{+} CD11c- cells, then CD8+ CD4- cells. Sorted cells were then further pooled and passed over a sample cartridge for the BD Rhapsody to trap single cells. Processing for RNA isolation and cDNA library preparation were carried out according to manufacturer's instructions.

CD8 qPCR: splenocytes were isolated from the spleens of A20$^{\Delta mg}$ mice and control mice through mechanical dissociation. Brains from A20$^{\Delta mg}$ mice were processed as described above. CD8^{+} T cells were isolated through negative selection using the CD8a^{+} T cell isolation kit from Miltenyi, according to manufacturer's instructions. The flow-through from the CNS was further incubated with anti-CD45 beads from Miltenyi to positively select for CD8^{+} T cells and remove neural cells which are not removed with the previous negative selection step. Isolated CD8 T cells were then lysed in lysis buffer from QIAGEN and frozen at −80°C until RNA-extraction was performed.

RNA extraction, qPCR and sequencing

Sorted microglia were processed for RNA extraction using the RNeasy Plus mini kit (QIAGEN) according to manufacturer's instructions. RNA quality and concentration were measured using a NanoDrop™ (Thermo Fisher Scientific). For qPCR, cDNA was prepared from total RNA using QuantiTect Reverse Transcription kit (QIAGEN).

For sequencing, RNA quality and integrity was determined using a Qbit 2.0 (Invitrogen, Thermo Fisher Scientific) and RNA quality was assessed on a RNA 6000 Pico by Bioanalyzer 2100 (Agilent). Only samples with a RIN value of 7.0 and above were taken for further processing. Barcoded mRNA-seq cDNA libraries were prepared from 10ng of total RNA using NEBNext® Poly (A) mRNA Magnetic Isolation Module and NEBNext® Ultra II RNA Library Prep Kit for Illumina® according to the manual. All quality controls were done using Invitrogen's Qubit HS assay and fragment size was determined using Agilent's 2100 Bioanalyzer HS DNA assay. Barcoded RNA-Seq libraries were onboard clustered using HiSeq® Rapid SR Cluster Kit v2 using 8pM and 59bps were sequenced

on the Illumina HiSeq2500 using HiSeq® Rapid SBS Kit v2 (59 Cycle). The raw output data of the HiSeq was preprocessed according to the Illumina standard protocol.

RNA sequencing: analysis

Quality control on the sequencing data was performed with the FastQC tool and the Qorts suite. RNA sequencing reads were aligned to the ENSEMBL Mus_musculus.GRCm38 as a reference genome. The corresponding annotation (ENSEMBL v76) was also retrieved from ENSEMBL FTP website. The STAR aligner (version 2.4.0j; Dobin et al., 2013) was used to perform mapping to the reference genome. Alignments were processed with the featureCounts function of the Rsubread package, using the annotation file also used for supporting the alignment. Differential expression analysis was performed with DESeq2 package (version 1.22.1; Love et al., 2014), setting the false discovery rate (FDR) to 0.05. Accurate estimation of the effect sizes (in terms of log fold change) is performed using the apeglm shrinkage estimator (version 1.4.1; Zhu et al., 2018).

Gene expression profiles were plotted as heatmaps (color-coded z-scores for the expression values, after regularized logarithm transformation) with the R programming language and the pheatmap package (version 1.0.10). Principal component analysis was performed using the pcaExplorer package (version 2.8.0; Marini and Binder, 2017). To highlight the differences of the expression values between the two groups MA-Plots were generated with the R programming language and the plotly package (version 4.8.0). For gene set enrichment analysis (GSEA), rank scores for differential mRNA expression between $A20^{\Delta mg}$ and $A20^{fl/wt}$ $Cx3cr1\text{-}Cre^{ERT2/+}$ groups were calculated as -log10 (p value) multiplied by the sign of the fold change such that upregulated genes had positive scores and downregulated genes had negative scores. The java GSEA Desktop Application v2.2.1 was used to run the analysis and evaluate enriched GO and KEGG pathways. Normalized Enrichment Scores were calculated using the function GseaPreranked. Enrichment analysis for Gene Ontology; Ashburner et al., 2000) (GO) was visualized using the Enrichment Map plugin (http://www.baderlab.org/Software/EnrichmentMap) for Cytoscape (version 3.6.0) (https://cytoscape.org/). Default settings were used for visualization, using p value < 0.01 and q-value < 0.01 and an overlap coefficient cut-off of 0.5. Enriched GO terms were uploaded to Enrichment Map, and a network graph was constructed. Nodes represent enriched GO terms and edges the degree of similarity between them using the overlap coefficient.

QUANTIFICATION AND STATISTICAL ANALYSIS

Data are shown either as mean ± SD or ± SEM, as indicated in the figure legends. For comparison of two groups, we performed Mann-Whitney Test or multiple t test with the Holm-Sidak method as indicated in the figure legends. Sholl analysis was analyzed by 2-way ANOVA with Sidak's Multiple Comparison's test. Significance is indicated as follows: * $p < 0.05$, ** $p < 0.01$, ***$p < 0.001$.

DATA AND CODE AVAILABILITY

The RNA-seq data presented in this manuscript has been deposited in NCBI's Gene Expression Omnibus (Edgar et al., 2002) and are accessible through GEO series accession number GSE123033 (https://www.ncbi.nlm.nih.gov/geo/query/acc.cgi?acc=GSE123033).